The Astrophysical Journal, 776:85 (19pp), 2013 October 20 doi:10.1088/0004-637X/776/2/85

ATMOSPHERIC DYNAMICS OF BROWN DWARFS AND DIRECTLY IMAGED GIANT PLANETS

Adam P. Showman[1] and Yohai Kaspi[2]
[1] Department of Planetary Sciences and Lunar and Planetary Laboratory, The University of Arizona, 1629 University Boulevard, Tucson, AZ 85721, USA; showman@lpl.arizona.edu
[2] Center for Planetary Science, Weizmann Institute of Science, Rehovot, Israel
Received 2012 October 27; accepted 2013 July 15; published 2013 October 1

ABSTRACT

A variety of observations provide evidence for vigorous motion in the atmospheres of brown dwarfs and directly imaged giant planets. Motivated by these observations, we examine the dynamical regime of the circulation in the atmospheres and interiors of these objects. Brown dwarfs rotate rapidly, and for plausible wind speeds, the flow at large scales will be rotationally dominated. We present three-dimensional, global, numerical simulations of convection in the interior, which demonstrate that at large scales, the convection aligns in the direction parallel to the rotation axis. Convection occurs more efficiently at high latitudes than low latitudes, leading to systematic equator-to-pole temperature differences that may reach ∼1 K near the top of the convection zone. The interaction of convection with the overlying, stably stratified atmosphere will generate a wealth of atmospheric waves, and we argue that, as in the stratospheres of planets in the solar system, the interaction of these waves with the mean flow will cause a significant atmospheric circulation at regional to global scales. At large scales, this should consist of stratified turbulence (possibly organizing into coherent structures such as vortices and jets) and an accompanying overturning circulation. We present an approximate analytic theory of this circulation, which predicts characteristic horizontal temperature variations of several to ∼50 K, horizontal wind speeds of ∼10–300 m s^{-1}, and vertical velocities that advect air over a scale height in $\sim 10^5$–10^6 s. This vertical mixing may help to explain the chemical disequilibrium observed on some brown dwarfs. Moreover, the implied large-scale organization of temperature perturbations and vertical velocities suggests that near the L/T transition, patchy clouds can form near the photosphere, helping to explain recent observations of brown-dwarf variability in the near-IR.

Key words: brown dwarfs – convection – methods: numerical – stars: low-mass – turbulence – waves

Online-only material: color figures

1. INTRODUCTION

Since the discovery of brown dwarfs beginning in the mid-1990s, our understanding of the atmospheric structure of these objects has grown ever more sophisticated. Approximately 1000 brown dwarfs, and a handful of directly imaged planets, have now been discovered. Observational acquisition of infrared (IR) spectra for many of these objects has allowed the definition of the L, T, and Y spectral classes (e.g., Kirkpatrick 2005; Cushing et al. 2011). The theory for these objects now encompasses a broad understanding of their evolution, radii, luminosity, molecular composition, spectra, and colors, and includes prescriptions for condensate formation and rainout, surface patchiness, and disequilibrium chemistry. Notably, however, these theoretical advances have relied heavily on one-dimensional (1D) models for the atmospheric radiative transfer and interior evolution (for an early review, see Burrows et al. 2001). By comparison, little effort has been made to understand the global, three-dimensional (3D) atmospheric dynamics of these substellar bodies.

Yet there is increasing evidence that brown dwarfs exhibit vigorous atmospheric circulations. This evidence falls into three main classes. First, L dwarfs, particularly of later spectral type, show a reddening of near-infrared (e.g., $J-K$) colors that indicate the presence of silicate clouds in the visible atmospheres (e.g., Kirkpatrick et al. 1999; Kirkpatrick 2005; Chabrier et al. 2000; Tsuji 2002; Cushing et al. 2006; Knapp et al. 2004). Since cloud particles would gravitationally settle in the absence of dynamics, such clouds imply the presence of atmospheric vertical mixing necessary to keep the particles suspended. In the cooler T dwarfs, the condensation occurs progressively deeper and, for objects with sufficiently low effective temperature, eventually no longer influences the infrared spectrum. However, the L/T transition itself remains poorly understood; it occurs over a surprisingly small range of effective temperature and accompanies a *J*-band brightening, which are not easily captured by standard 1D models (Chabrier et al. 2000; Allard et al. 2001; Burrows et al. 2006b; Saumon & Marley 2008). Hypotheses that have been put forward to resolve this discrepancy are that across the transition, the cloud sedimentation efficiency changes (Knapp et al. 2004) or that the clouds become patchy, allowing contributions from both cloudy and cloud-free regions to affect the disk-integrated emergent spectrum (Ackerman & Marley 2001; Burgasser et al. 2002; Marley et al. 2010). In both cases, a role for atmospheric dynamics in modulating the clouds is implicated.

A second line of evidence for atmospheric circulation comes from chemical disequilibrium of CO, CH_4, and NH_3 inferred for many cool brown dwarfs. Late T dwarfs have sufficiently cool atmospheres that the preferred chemical-equilibrium forms of carbon and nitrogen near the photosphere are CH_4 and NH_3, respectively; in contrast, CO and N_2 dominate under the high-pressure and high-temperature regions at depth. Fitting of IR spectra to radiative transfer models shows that near the photosphere, many T dwarfs exhibit an overabundance of CO and an underabundance of NH_3 relative to chemical equilibrium. This can be attributed to vertical transport of CO-rich and NH_3-poor air from depth and the subsequent chemical quenching of these disequilibrium mixing ratios due to the long chemical interconversion timescales in the low-pressure, low-temperature regions near the photosphere. This story was first worked out

for CO on Jupiter (Prinn & Barshay 1977; Bézard et al. 2002; Visscher & Moses 2011) and then for both CO and NH_3 on Gl 229b (Fegley & Lodders 1996; Noll et al. 1997; Griffith & Yelle 1999; Saumon et al. 2000). Subsequently, chemical disequilibrium and vertical mixing have been inferred in the atmospheres of a wide range of T dwarfs (Saumon et al. 2006, 2007; Hubeny & Burrows 2007; Leggett et al. 2007a, 2007b, 2008, 2010; Stephens et al. 2009).

Third, recent near-IR photometric observations demonstrate that several brown dwarfs near the L/T transition exhibit large-amplitude variability over rotational timescales, probably due to cloudy and relatively cloud-free patches rotating in and out of view. The possibility of weather on brown dwarfs has long motivated searches for variability. Recently, Artigau et al. (2009) observed the T2.5 dwarf SIMP0136 in the J and K_s bands and found peak-to-peak modulations of ∼5% (∼50 mmag) throughout the inferred 2.4 hr rotation period. Radigan et al. (2012) observed the T1.5 dwarf 2M2139 in J, H, and K_s and found peak-to-peak variations of up to ∼25% with an inferred rotation period of either 7.7 or 15.4 hr. The relative amplitudes of the variability at J, H, and K_s place strong constraints on the cloud and thermal structure associated with the variability. These authors considered models where the variability resulted from lateral variations in effective temperature alone (with no variations in the cloud properties), lateral variations in the cloud properties alone (with no variation in effective temperature), and lateral variations in both temperature and cloud properties. The observations rule out models with a uniform cloud deck and instead strongly favor models with significant lateral variations in both cloud opacity and effective temperature; the relatively cloud-free regions exhibit effective temperatures ∼100–400 K greater than the cloudier regions. This suggests a picture with spatially distinct regions of lower and higher condensate opacity, where radiation escapes to space from lower-pressure, cooler levels in the high-opacity regions and deeper, warmer levels in the low-opacity regions. The observations of Artigau et al. (2009) and Radigan et al. (2012) both show that the light curves vary significantly over intervals of several Earth days, indicating that the shape, orientation, or relative positions of the low- and high-condensate opacity regions evolve over timescales of days.

In addition to these observations of field brown dwarfs, growing numbers of young, hot extrasolar giant planets (EGPs) are being imaged and characterized. Prominent discoveries include planetary-mass companions to β Pic, 2M1207, and HR 8799. Multi-band photometry already indicates that 2M1207b and several of the HR 8799 planets exhibit clouds and probably disequilibrium chemistry similar to that inferred on brown dwarfs (Hinz et al. 2010; Bowler et al. 2010; Currie et al. 2011; Galicher et al. 2011; Skemer et al. 2011; Madhusudhan et al. 2011; Barman et al. 2011a, 2011b; Marley et al. 2012). With effective temperatures exceeding ∼1000 K, these planets radiate IR fluxes $\gtrsim 10^5$ W m^{-2}, orders of magnitude greater than the flux received by their primary star. Stellar irradiation is therefore negligible to their dynamics. From a meteorology perspective, this population of bodies will therefore resemble low-mass, low-gravity versions of free-floating brown dwarfs. With next-generation telescope facilities, including the Gemini Planet Imager and SPHERE, significant numbers of new planets will be discovered, greatly opening our ability to probe planetary meteorology at the outer edge of stellar systems.

These existing and upcoming observations provide strong motivation for investigating the global atmospheric dynamics of brown dwarfs and directly imaged planets. As yet, however, no investigations of the global atmospheric circulation of brown dwarfs have been performed. The only study of brown-dwarf atmospheric dynamics published to date is that of Freytag et al. (2010), who performed two-dimensional, non-rotating convection simulations in a box ∼400 km wide by ∼150 km tall. Their study provides valuable insights into the role of convectively generated small-scale gravity waves in causing vertical mixing. Nevertheless, dynamics on scales of tens to hundreds of kilometers differs substantially from that on global scales of 10^4–10^5 km, and thus, for understanding the global-scale circulation—including the implications for variability—it is essential to consider global-scale models.

Here, we aim to fill this gap by presenting the first global-scale models of brown-dwarf atmospheric dynamics. Rotation periods of L and T dwarfs inferred from spectral line broadening range from ∼2 to 12 hr (Zapatero Osorio et al. 2006; Reiners & Basri 2008), in line with the periods of SIMP0136 and 2M2139 inferred from light-curve modulation (Artigau et al. 2009; Radigan et al. 2012). We will show that at these periods, rotation dominates the global-scale dynamics and will constitute an overriding factor in controlling the 3D wind and temperature structure. We first present theoretical arguments to highlight the fundamental dynamical regime in which brown dwarfs lie, to show how rotation organizes the large-scale wind, establishes systematic temperature differences, and shapes the convective velocities (Section 2). We next present global, 3D numerical simulations of the interior convection of brown dwarfs that confirm our theoretical arguments and provide insights into the detailed, time-evolving global wind and temperature patterns and dynamical timescales (Section 3). We then consider the dynamics of the stably stratified atmosphere that overlies the convective interior, demonstrating how large-scale vortices and/or zonal[3] jets are likely to emerge from interactions with the interior (Section 4). Next, we consider observational implications, since IR radiation to space typically occurs from within this stratified layer, and hence infrared spectra and light curves are strongly shaped by its dynamics (Section 5). The final section gives our conclusions (Section 6).

We emphasize that our goal is to provide a theoretical foundation for understanding the atmospheric dynamics of rapidly rotating, ultracool dwarfs and young EGPs, broadly defined. As such, we emphasize dynamical considerations and intentionally simplify our models by excluding clouds, chemistry, and detailed representation of radiative transfer. This provides a clean environment in which to identify key dynamical processes and construct a theoretical foundation for more realistic studies that will surely follow.

2. BACKGROUND THEORY: APPLICATION TO BROWN DWARFS

Here, we review basic concepts in atmospheric fluid dynamics and apply them to brown dwarfs to understand the large-scale structure of the flow.

2.1. Importance of Rotation

Brown dwarfs rotate rapidly, and this will exert a major influence on their atmospheric dynamics. To demonstrate, consider

[3] Zonal refers to the east–west (longitudinal) direction, whereas meridional refers to the north–south (latitudinal) direction. Zonal and meridional winds are winds in the eastward and northward directions, respectively. Zonal jets refer to atmospheric jet streams oriented in the east–west direction.

the momentum equation for a rotating fluid, which is given in the rotating reference frame of the brown dwarf by

$$\frac{d\mathbf{v}}{dt} + 2\boldsymbol{\Omega} \times \mathbf{v} = -\frac{1}{\rho}\nabla p - \nabla\Phi, \quad (1)$$

where $d\mathbf{v}/dt = \partial\mathbf{v}/\partial t + \mathbf{v}\cdot\nabla\mathbf{v}$ is the material derivative, $\mathbf{v}$ is the 3D velocity vector, $\boldsymbol{\Omega}$ is the planetary rotation vector, Φ is a force potential which includes both the gravitational and centrifugal accelerations, ∇ is the 3D gradient operator, t is time, and p and ρ are the pressure and density fields, respectively (Pedlosky 1987). For the purpose of this discussion we will assume that the dynamics are inviscid. We also for the present neglect the Lorentz force, as appropriate for the atmospheres and molecular envelopes of cool brown dwarfs; nevertheless, the Lorentz force will be crucial in the deep interior, and we will return to a discussion of it in Section 3.3.

The nature of the flow depends on the Rossby number, given by the ratio of the advective and Coriolis accelerations, $\mathrm{Ro} = U/\Omega L$, where U is a characteristic wind speed, L is a characteristic length scale of the flow, and Ω is the rotation rate (2π over the rotation period). If $\mathrm{Ro} \ll 1$, the flow is rotationally dominated; if $\mathrm{Ro} \sim 1$, rotation is important but not dominant, while if $\mathrm{Ro} \gg 1$, rotation plays a minor role (see, e.g., Vallis 2006, p. 84). Because of their fast rotation rates, Jupiter, Saturn, Uranus, and Neptune, as well as the extratropical atmospheres of Earth and Mars, all exhibit $\mathrm{Ro} \ll 1$ at large scales; the only solar-system atmospheres where rotation does not dominate are those of Titan and Venus.

Estimating Ro for brown dwarfs requires knowledge of wind speeds and flow length scales, which are unknown.[4] Nevertheless, Artigau et al. (2009) show that if the evolution of their light-curve shapes over intervals of days is interpreted as differential zonal advection of quasi-static features by a latitude-dependent zonal wind, the implied differential rotation is ∼1%, which for the 2.4 hr rotation period of SIMP0136 implies a zonal wind speed of ∼300–500 m s^{-1} depending on the latitude of the features. A similar analysis by Radigan et al. (2012) suggests a possible zonal wind speed of ∼45 m s^{-1} for 2M2139, although they caution that this estimate relies on rather tentative assumptions. Interestingly, these values bracket the range of wind speeds measured for the giant planets in the solar system, which range from typical speeds of ∼30 m s^{-1} on Jupiter to ∼300 m s^{-1} on Neptune (e.g., Ingersoll 1990).[5] Later, we show that the large-scale winds in the convective interior of a brown dwarf are likely to be weak (Section 3.3), but that winds potentially exceeding $\sim 10^2$ m s^{-1} could develop in the stratified atmosphere (Section 4).

Regarding length scale, the fact that SIMP0136 and 2M2139 exhibit large-amplitude variability hints that atmospheric features could be near-global in size (particularly for 2M2139, where variability reaches 25%). This would imply $L \sim R_J \sim 7 \times 10^7$ m, where R_J is Jupiter's radius. On the other hand, only a small fraction of brown dwarfs exhibit such large variability, and it is possible that length scales are typically smaller; for example, $L \sim 10^7$ m on Jupiter, Saturn, Uranus, and Neptune.

[4] Here, we seek to understand the global-scale flow, and the appropriate values are therefore not the convective velocities and length scales but the wind speeds and length scales associated with any organized jets (i.e., zonal flows) and vortices that may exist.

[5] The *maximum* observed speeds, expressed as a difference between the peak eastward and peak westward zonal winds, are several times these typical values, reaching ∼200 m s^{-1} on Jupiter and ∼600 m s^{-1} on Neptune.

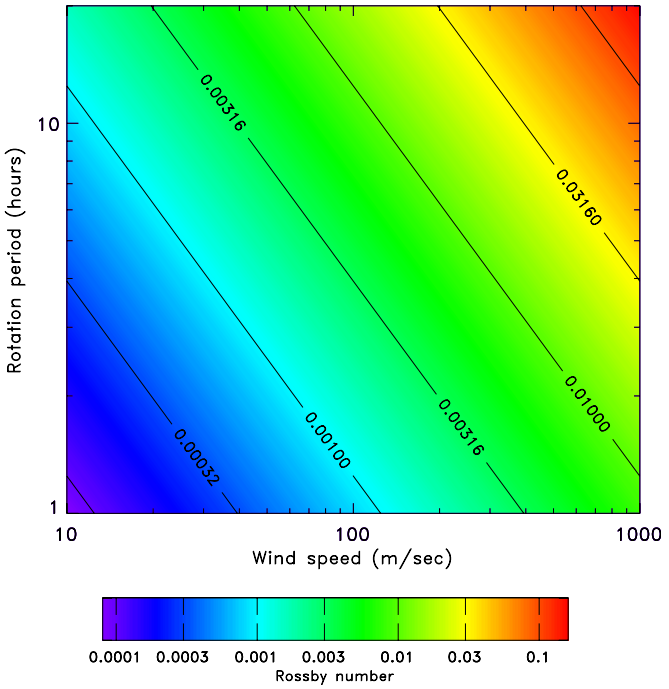

Figure 1. Rossby numbers expected on brown dwarfs as a function of rotation period and characteristic wind speed, assuming that dynamical features are global in scale (length equals one Jupiter radius). Rossby numbers range from $\sim 10^{-4}$ to 0.1, indicating that the regional- and global-scale dynamics in brown-dwarf atmospheres will be rotationally dominated over a wide range of parameters. Contour levels are in half-decade increments from 0.1 at the upper right to 0.0001 at the lower left.

(A color version of this figure is available in the online journal.)

Adopting length scales $L \sim 10^7$–10^8 m, wind speeds $U \sim$ 10–1000 m s^{-1}, and rotation rates of 2–10 hr yields Rossby numbers ranging from 0.0001 to 0.4. Figure 1 shows the Rossby number as a function of wind speed and rotation period for the case of global-scale flows. The values are much less than one everywhere except for the largest wind speeds and slowest rotation periods considered. This implies that, in general, the large-scale circulation on brown dwarfs will be rotationally dominated. The $\mathrm{Ro} \ll 1$ condition on brown dwarfs implies that the flow is geostrophically balanced, that is, the primary balance in the momentum equation is between Coriolis and pressure-gradient forces (Pedlosky 1987).

2.2. Organization of Flow

Significant insight into the flow structure can be obtained from the vorticity balance. Taking the curl of (1) gives a vorticity equation of the form (e.g., Pedlosky 1987)

$$\frac{\partial\omega}{\partial t} + (2\boldsymbol{\Omega} + \omega)\cdot\nabla\mathbf{v} - (2\boldsymbol{\Omega} + \omega)\,\nabla\cdot\mathbf{v} = -\frac{\nabla\rho\times\nabla p}{\rho^2}, \quad (2)$$

where $\omega = \nabla\times\mathbf{v}$ is the relative vorticity. The term on the right side, called the baroclinic term, is nonzero when density varies on constant-pressure surfaces. Note that since ω scales as U/L, the ratio $\omega/\Omega \sim \mathrm{Ro}$, and the time-derivative term is generally of the order of Ro smaller in magnitude than the second and third terms on the left side. Taking $\mathrm{Ro} \ll 1$, appropriate to the flow on a brown dwarf, yields a leading-order vorticity balance given by

$$2\boldsymbol{\Omega}\cdot\nabla\mathbf{v} - 2\Omega\nabla\cdot\mathbf{v} = -\frac{\nabla\rho\times\nabla p}{\rho^2}. \quad (3)$$

One might expect that convection homogenizes the entropy within the convection zone, in which case density does not vary on isobars and $\nabla\rho \times \nabla p = 0$. This is called a barotropic flow. In this case, Equation (3) simply becomes the compressible-fluid generalization of the Taylor–Proudman theorem, which, expressed in a cylindrical coordinate system centered on the rotation axis, is

$$\frac{\partial u}{\partial \hat{z}} = \frac{\partial v_\perp}{\partial \hat{z}} = 0 \tag{4}$$

$$\nabla_\perp \cdot \mathbf{v}_\perp = 0, \tag{5}$$

where $\hat{z}$ is the direction parallel to the rotation axis, u is the azimuthal (zonal) velocity, $v_\perp$ is the velocity toward/away from the rotation axis, $\mathbf{v}_\perp = (u, v_\perp)$ is the velocity in the plane perpendicular to the rotation axis, and $\nabla_\perp$ is the gradient operator in the plane perpendicular to the rotation axis. The theorem states that if the flow has a small Rossby number and is inviscid and barotropic, the fluid motion will be completely two-dimensional, and therefore there will be no variation in the fluid velocity along the direction of the axis of rotation. The fluid then moves in columns aligned with the rotation axis. Note that no constant-density assumption was made; Equations (4) and (5) hold in a barotropic, geostrophic, low-viscosity fluid even if the density varies by orders of magnitude across the system.

Within a spherical planet or brown dwarf, such columns can easily move in the zonal (east–west) direction. However, the columns cannot easily move toward or away from the rotation axis, because this changes the length of the columns and the local density within them, both of which induce non-zero $\nabla_\perp \cdot \mathbf{v}_\perp$ that violate the theorem. For such a barotropic fluid, the predominant planetary-scale circulation therefore consists of zonal (east–west) wind whose speed varies minimally in the direction along the rotation axis; by comparison, the north–south flow is weak. Of course, the theorem is only valid to order Ro, and so motions toward/away from the rotation axis—as well as motions parallel to the fluid columns—can occur, but only with amplitudes ~Ro less than that of the primary zonal flow.[6]

In reality, turbulent convection results in horizontal entropy gradients, and therefore the fluid is not in a barotropic state, leading to a non-vanishing term on the right side of Equation (3). As a result, shear can develop along the $\hat{z}$ direction. Considering the zonal component of Equation (3) yields

$$2\Omega \frac{\partial u}{\partial \hat{z}} = -\frac{\nabla\rho \times \nabla p}{\rho^2} \cdot \hat{\lambda}, \tag{6}$$

where $\hat{\lambda}$ is the unit vector in the longitudinal direction. If the flow exhibits minimal variation in longitude, then it can be shown that $|\nabla\rho \times \nabla p| = |\nabla p|(\partial\rho/\partial y)_p$, where y is northward distance. Since $|\nabla p|$ is overwhelmingly dominated by the hydrostatic component, we have to good approximation (Showman et al. 2010)

$$2\Omega \frac{\partial u}{\partial \hat{z}} = \frac{g}{\rho r}\left(\frac{\partial \rho}{\partial \phi}\right)_p, \tag{7}$$

where ϕ is latitude, g is gravity and r is radial distance from the center of the planet. Thus, variations in the geostrophic wind along $\hat{z}$ must be accompanied by variations in density on isobars. This relation, well known in atmospheric dynamics, is called the thermal-wind equation.

By itself, however, the preceding theory gives little insight into the spatial organization—columnar or not—of the internal entropy perturbations and any thermal-wind shear that accompanies them. An alternative point of view that sheds light on this issue is to consider the angular momentum budget. The angular momentum per unit mass about the rotation axis is given by

$$M \equiv M_\Omega + M_u = \Omega r^2 \cos^2\phi + ur\cos\phi, \tag{8}$$

where the first and second terms represent the contributions due to the planetary rotation and winds in that rotating frame, respectively. Writing the zonal momentum equation in terms of angular momentum yields (e.g., Peixoto & Oort 1992, Chapter 11)

$$\rho \frac{dM}{dt} = -\frac{\partial p}{\partial \lambda}, \tag{9}$$

where λ is longitude. It is useful to decompose the pressure and density into contributions from a static, wind-free reference state and the deviations from that state due to dynamics. When wind speeds are much less than the speed of sound, these dynamical density and pressure perturbations are small, leading to a continuity equation $\nabla \cdot (\tilde{\rho}\mathbf{v}) = 0$, where $\tilde{\rho}$ is the reference density profile.[7] Motivated by the fact that the convective eddies drive a mean flow, we represent the dynamical variables as the sum of their zonal means (denoted by overbars) and the deviations therefrom (denoted by primes), such that $M = \overline{M} + M'$, $\mathbf{v} = \overline{\mathbf{v}} + \mathbf{v}'$, etc. Here, we refer to these overbarred quantities as the mean flow and the primed quantities as the eddies. Substituting these expressions into Equation (9) and zonal averaging leads to the zonal-mean momentum equation (see Kaspi et al. 2009)

$$\tilde{\rho}\frac{\partial \overline{M}}{\partial t} + \nabla \cdot (\tilde{\rho}\overline{\mathbf{v}}\,\overline{M}) + \nabla \cdot (\tilde{\rho}\overline{\mathbf{v}'M'}) = 0. \tag{10}$$

This equation states that temporal changes to the zonal-mean angular momentum at any given location (first term) can only result from advection of the zonal-mean angular momentum by the mean flow (second term) or changes in the zonal-mean angular momentum due to torques caused by eddy motions (third term). In a statistical steady state, $\overline{M}$ equilibrates and the equation simply becomes

$$\nabla \cdot (\tilde{\rho}\overline{\mathbf{v}}\,\overline{M}) + \nabla \cdot (\tilde{\rho}\overline{\mathbf{v}'M'}) = 0. \tag{11}$$

Since the ratio of M_u to M_Ω is essentially the Rossby number, it follows that for the Ro $\ll 1$ regime expected on a brown dwarf, $M \approx M_\Omega$. Thus, for a rapidly rotating brown dwarf, surfaces of constant angular momentum are nearly parallel to the axis of rotation. Using this result, along with the continuity equation, Equation (11) becomes

$$\overline{\mathbf{v}} \cdot \nabla M_\Omega = -\frac{1}{\tilde{\rho}}\nabla \cdot (\tilde{\rho}\overline{\mathbf{v}'M'}). \tag{12}$$

This result has major implications for the circulation on rapidly rotating giant planets and brown dwarfs. The equation

[6] Of course, at very small scales, the Rossby number exceeds unity and the convection at these small scales will not organize into columns (e.g., Glatzmaier et al. 2009). The columnar organization applies only at scales sufficiently large that Ro $\ll 1$.

[7] The reference density will generally be a function of radius. Note that this approximate continuity equation (essentially the anelastic approximation) filters sound waves from the system, which is a reasonable approximation as long as wind speeds are much less than the speed of sound.

implies that the mean flow, $\overline{\mathbf{v}}$, can only cross angular momentum surfaces in the presence of eddy correlations between $\mathbf{v}'$ and M' (such eddy correlations cause a torque that changes the zonal-mean angular momentum following the mean flow, as necessary for the mean flow to cross angular momentum surfaces). When such eddy effects are small, or if the flow is axisymmetric with no variation in longitude (for which $\mathbf{v}'$ and M' are zero by definition), then $\overline{\mathbf{v}} \cdot \nabla M_\Omega = 0$ (Liu & Schneider 2010). In such a situation, the mean flow must to leading order be parallel to surfaces of constant angular momentum (Busse 1976; Kaspi et al. 2009), and there can be no flow crossing these surfaces. This constraint places no limitation on the zonal-mean zonal flow, $\overline{u}$, but requires the meridional circulation $\overline{v}$ to be small. It is important to emphasize that this constraint differs from the Taylor–Proudman theorem, since it does not require the flow to be barotropic, nor does it state that $\overline{u}$ is independent of $\hat{z}$.

But how important are the eddy torques on the right-hand side of Equation (12)? At small Rossby number, the planetary rotation contains so much angular momentum that even in the presence of vigorous convection, eddy torques are unable to drive a rapid mean-meridional circulation; therefore, we still have $\overline{\mathbf{v}} \cdot \nabla M_\Omega \approx 0$ at leading order. To show this, we can estimate the timescale of the meridional circulation and compare it to the characteristic timescale for convection. The characteristic timescale for convection to traverse the interior is $\tau_{\rm conv} \sim D/w$, where D is a thickness of the layer in question (e.g., the planetary radius) and w is the characteristic convective speed. We can estimate the timescale for the mean flow to cross angular momentum contours as follows. The eddy correlation $\overline{\mathbf{v}'M'}$ is just $\overline{\mathbf{v}'u'r_\perp}$, where $r_\perp$ is the distance from the rotation axis. Under the assumption that the eddy velocities scale with the convective velocities w, we can write $\overline{\mathbf{v}'M'} \sim C r_\perp w^2$, where C is a correlation coefficient equal to one when u' and $\mathbf{v}'$ are perfectly correlated and equal to zero when u' and $\mathbf{v}'$ exhibit no correlation. To order of magnitude, Equation (12) then becomes

$$\overline{v}_\perp \Omega r_\perp \sim C w^2, \tag{13}$$

and the meridional velocity therefore has a characteristic magnitude

$$\overline{v}_\perp \sim \frac{C w^2}{\Omega r_\perp}. \tag{14}$$

Defining a timescale for the meridional circulation, $\tau_{\rm merid} = r_\perp/\overline{v}_\perp$, implies that

$$\tau_{\rm merid} \sim \tau_{\rm conv} \frac{r_\perp \Omega}{C w}, \tag{15}$$

which can be expressed as

$$\tau_{\rm merid} \sim \frac{\tau_{\rm conv}}{C\,{\rm Ro}_{\rm conv}}, \tag{16}$$

where ${\rm Ro}_{\rm conv} = w/r_\perp\Omega$ is a convective Rossby number giving the ratio of the convective velocities to the typical rotational velocity of the planet in inertial space. For typical brown dwarfs, where rotational velocities are tens of km s^{-1}, we expect ${\rm Ro}_{\rm conv} \ll 1$; given the expected convective velocities (see Section 3), we expect ${\rm Ro}_{\rm conv} \sim 10^{-5}$–$10^{-2}$. Therefore, the timescale for the meridional circulation is several orders of magnitude longer than the characteristic convection timescale.

This also means that the convective heat transport will be more efficient along (rather than across) surfaces of constant angular momentum. Figure 2 shows the onset of convection for an experiment driven by a constant heat flux at the bottom boundary. Two models are shown, a rapidly rotating case on the left and a slowly rotating case on the right. While for the larger Rossby number case the dominant driving force for the turbulent plumes is the buoyancy and therefore the plumes are driven away from the center of gravity, for the small Rossby number case the convection becomes aligned along the direction of the axis of rotating demonstrating the angular momentum constraint ($\mathbf{v}\cdot\nabla M_\Omega = 0$). Note that for the small Rossby number experiment, only close to the boundaries does the Rossby number approach one and therefore there the convective cells can close. Thus, rotation strongly modulates the heat transport from the interior of the brown dwarf at large scales.

Figure 2. Pedagogical illustration, using two anelastic models, of the importance of rotation in the brown-dwarf parameter regime. The left column shows a rapidly rotating model (10 hr rotation period), and the right column shows a slowly rotating model (2000 hr rotation period). A constant heat flux is applied at the bottom boundary, leading to convection. Both models are fully 3D simulations extending 360° in longitude and adopt Jovian-like radial profiles of density and thermal expansivity from the SCVH EOS. In each model, the top panel shows the transient initial stage soon after convection initiates, and the bottom panel shows the state after the convection is well developed. Colorscale denotes entropy perturbations at an arbitrary longitude, shown in the radius–latitude plane. Rotation vector points upward in the figure. In the slowly rotating case, rotation plays no role in the dynamics, whereas in the rapidly rotating case, the rotation forces the large-scale flow to align along columns parallel to the rotation axis.

(A color version of this figure is available in the online journal.)

3. THREE-DIMENSIONAL CIRCULATION MODEL OF CONVECTION-ZONE DYNAMICS

3.1. Model

We solve the fluid equations for a convecting, 3D, rotating brown dwarf. We adopt the anelastic system (e.g., Ogura & Phillips 1962; Gilman & Glatzmaier 1981; Ingersoll & Pollard 1982), which assumes that dynamics introduces only small perturbations of the density, entropy, and pressure from a specified reference state, which we here take to be isentropic. Dynamical density perturbations then enter the momentum equations in the buoyancy term but do not appear in the continuity equation; this has the effect of filtering acoustic waves from the system. The anelastic system is appropriate for the fluid interior of a brown dwarf, where dynamical perturbations of entropy, density, and pressure due to convection are expected to be modest and convection should lead to a nearly constant entropy throughout. Although this study represents its first application to brown dwarfs, the anelastic system has previously been used with great success for understanding convection in Jupiter and Saturn (Kaspi et al. 2009; Jones & Kuzanyan 2009; Glatzmaier et al. 2009; Showman et al. 2011) and stellar interiors (Miesch & Toomre 2009 and references therein).

Our particular implementation is that of Kaspi et al. (2009). The momentum, continuity, and energy equations, respectively, are given by

$$\frac{\partial \mathbf{v}}{\partial t} + (2\mathbf{\Omega} + \omega) \times \mathbf{v} = -\frac{1}{\tilde{\rho}} \nabla p' - \frac{\rho'}{\tilde{\rho}} \nabla \Phi - \frac{1}{2} \nabla \mathbf{v}^2 + \nu \nabla^2 \mathbf{v} \quad (17)$$

$$\nabla \cdot (\tilde{\rho} \mathbf{v}) = 0 \quad (18)$$

$$\frac{\partial s'}{\partial t} + \frac{1}{\tilde{\rho}} \nabla \cdot (\tilde{\rho} \mathbf{v} s') - \frac{1}{\tilde{\rho}} \nabla \cdot (\tilde{\rho} \kappa \nabla s') = \frac{Q}{\tilde{T}}, \quad (19)$$

where Q is thermodynamic heating/cooling per mass, ν is the kinematic viscosity, κ is the thermal diffusivity, and other quantities are as defined previously. Here, both ν and κ are taken as constants and are intended to parameterize small-scale eddy mixing. The quantities $\tilde{\rho}(r)$, $\tilde{p}(r)$, and $\tilde{T}(r)$ are the radially varying reference profiles of density, pressure, and temperature, respectively; ρ' and p' are the deviations of the density and pressure from their local reference values, such that the total pressure and density are $\rho = \tilde{\rho} + \rho'$ and $p = \tilde{p} + p'$. Likewise, s' is the deviation of entropy from its reference state value.

The system is closed with an equation of state (EOS), which enters through the reference profiles and through the relationship between the density, entropy, and pressure perturbations in the anelastic system

$$\frac{\rho'}{\tilde{\rho}} = \frac{1}{\tilde{\rho}} \left(\frac{\partial \rho}{\partial s} \right)_p s' + \frac{1}{\tilde{\rho}} \left(\frac{\partial \rho}{\partial p} \right)_s p' \equiv -\alpha_s s' + \beta p', \quad (20)$$

where α_s and β are the radially varying isobaric entropy expansion coefficient and isentropic compressibility, respectively, along the model's radially varying reference profile. Here, we adopt the SCVH EOS for hydrogen–helium mixtures (Saumon et al. 1995). Given a specified brown-dwarf mass and internal entropy, and the assumption that the reference state is in hydrostatic balance,[8] this EOS allows us to calculate the radially varying reference profiles $\tilde{\rho}$, $\tilde{p}$, and $\tilde{T}$ (e.g., Guillot & Morel 1995; Guillot et al. 2004), as well as the radial profiles of α_s and β along the reference adiabat. The gravitational acceleration in the model varies radially, which we determine by integrating this basic state radially. See Kaspi et al. (2009, Figure 2) for the resulting radial profiles of density, temperature, pressure, gravity, thermal expansion coefficient, and specific heat used in the model.

Many studies of convection in rotating spherical shells force the system by passing a heat flux through impermeable upper and lower boundaries, with either a constant-temperature or constant-heat-flux boundary condition (e.g., Christensen 2001, 2002; Aurnou & Olson 2001; Heimpel et al. 2005 and many others). However, this is unrealistic in the context of a substellar object. At high Rayleigh numbers, passing a heat flux through the model boundaries will lead to thin hot and cold boundary layers at the bottom and top boundaries, respectively, which detach and form hot and cold convective plumes that in some cases can dominate the dynamics. Because real brown dwarfs are fluid throughout, the bottom boundary layer, in particular, is unrealistic. Instead, we force the system by imposing a vertically distributed source of internal heating and cooling throughout the bottom and top portions of the domain, respectively, thus allowing outward convective transport of heat without the development of artificial boundary layers (for more detail see Kaspi et al. 2009).[9] The top and bottom thermal boundary conditions correspond to zero heat flux. The top and bottom mechanical boundary conditions are impermeable in radial velocity and free-slip in horizontal velocity.

We solve the equations in spherical geometry using the state-of-the-art circulation model MITgcm (Adcroft et al. 2004), which Kaspi (2008) adapted for anelastic simulations of the deep convective envelopes of giant planets. The equations are solved using a finite-volume discretization on a staggered Arakawa C grid (Arakawa & Lamb 1977) in longitude and latitude. Our typical resolution is 1° in longitude and latitude with 120 vertical levels spaced to give enhanced resolution near the top of the domain where the pressure and density scale heights are the smallest (see Kaspi et al. 2009). Most models extend the full 360° in longitude and in latitude from 80°S to 80°N. For some parameter variations, we performed simulations in sectors 90° of longitude wide (using a periodic boundary condition between the eastern and western boundaries) with a resolution of 2° of longitude and latitude and 120 vertical levels. For all models, the outer and inner boundaries are spherical surfaces with radii of $1R_J$ and $0.5R_J$, respectively. This choice of inner boundary is sufficiently deep to minimize any artificial effect of the lower boundary on the surface dynamics. We generally use a Jupiter-like interior reference profile with a pressure at the outer surface of 1 bar and 20 Mbar at the bottom boundary. The interior reference density varies by a factor of over 10^4 from the 1 bar level to the deep interior (see Kaspi et al. 2009). All simulations are spun up from rest using an initial thermal profile

[8] We emphasize that the dynamical model itself is non-hydrostatic; hydrostatic balance is used only in defining the reference state.

[9] Real brown dwarfs of course do not have substantial internal heat sources (the burning of deuterium not playing a role except in the most massive objects) but rather decrease in entropy very gradually over multi-Byr timescales. Thus, ideally, one would like to set up the problem with a heat sink near the top (i.e., cooling) and no heat source near the bottom, thereby allowing the internal entropy to decline with time in a brown-dwarf-like fashion. The difficulty is that due to computational limitations, achieving steady state requires the system to be overforced (Showman et al. 2011), and without a source of energy near the bottom the interior entropy would decline unrealistically rapidly. Adding a heat source near the bottom, as we have done, allows the global-mean interior entropy to be essentially constant over dynamical timescales, consistent with expectations for brown dwarfs.

corresponding to the reference profile and are integrated until a statistical steady state is achieved.

3.2. Results: Convective and Thermal Structure

We perform simulations using rotation periods ranging from 3 to 200 hr (spanning the typical range observed for brown dwarfs), as well as an additional sequence of parameter variations adopting rotation periods as long as 2000 hr, to illustrate the effect of rotation on the dynamics.

Before presenting models for fully equilibrated brown dwarfs, we first demonstrate with a pedagogical example the crucial importance that rotation plays in the brown-dwarf parameter regime. Figure 2 depicts the temperature structure during the spin-up phase for two models that are identical except for the rotation period, which is 2000 hr in the model on the right and 10 hr for the model on the left. The models in Figure 2 are not intended to be realistic brown-dwarf models (for example, they are forced by a heat flux from the bottom boundary, which is not realistic in the context of a brown dwarfs) but are instead simply an illustration of the importance of rotation in the brown-dwarf parameter regime. Nevertheless, the models do have a realistic Jovian interior structure, with density increasing by a factor of $\sim 10^4$ from the interior to the exterior.

In the slowly rotating model (right panels of Figure 2), the Coriolis forces are sufficiently weak that the Rossby number is $\gtrsim 1$, so that rotation plays a negligible role in the dynamics. Convective plumes rise from the lower boundary and ascend quasi-radially toward the outer boundary. The plumes are equally able to radially traverse the domain whether they emanate from the polar or equatorial regions, and to zeroth order, the convection appears to be isotropic.

In contrast, the rapidly rotating model exhibits Ro $\ll 1$ and is thus rotationally dominated (Figure 2, left panels). As predicted by the theory in Section 2, the convection develops a columnar structure. Plumes that emerge in the polar regions can ascend and descend radially while remaining at nearly constant distance from the rotation axis; they therefore easily traverse the domain. However, plumes forming at lower latitudes cannot easily cross the domain because doing so requires them to change distance significantly from the rotation axis. In a Ro $\ll 1$ flow, angular momentum is not homogenized and lines of constant angular momentum are nearly parallel to the rotation axis. As a result, moving toward or away from the rotation axis can only be achieved by significantly increasing the angular momentum of ascending fluid parcels or decreasing the angular momentum of descending fluid parcels. The timescale for this angular momentum exchange is longer than the typical convection timescale for plumes to traverse the domain, and thus convection toward or away from the rotation axis is less efficient. Therefore, as expected from Section 2, rotation imposes on the flow a columnar structure.

Rotation strongly affects the vertical convective velocities as well. To order of magnitude, convective velocities w and temperature perturbations δT relate to the convective heat flux F as

$$F \sim \rho w c_p \delta T, \tag{21}$$

where c_p is specific heat at constant pressure and ρ is the local density. Convective temperature perturbations relate to convective density perturbations $\delta\rho$ via $\alpha\,\delta T \sim \delta\rho/\rho$, where α is thermal expansivity. The standard non-rotating mixing-length scaling results from assuming that buoyancy forces $g\,\delta\rho/\rho$ cause free acceleration of convective plumes over a mixing length l,

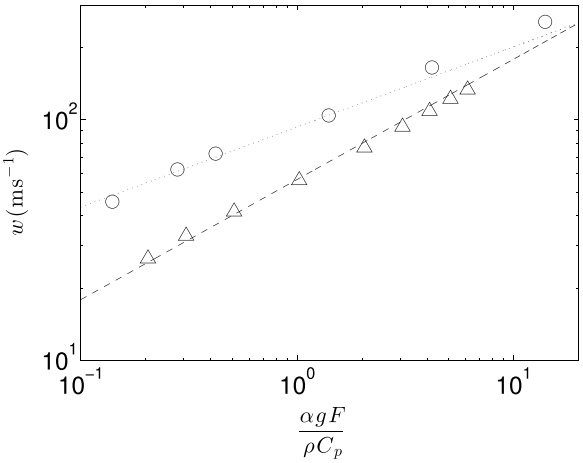

Figure 3. Vertical (i.e., radial) velocities for brown-dwarf convection models showing that rotation significantly affects the convective velocities. Each symbol shows the domain-averaged, mass-weighted rms vertical wind speed versus the mass-weighted mean buoyancy flux $\alpha g F/\rho c_p$ (units $\mathrm{m^2\,s^{-3}}$) for a given numerical integration. The circles show slowly rotating models (rotation period 100 hr), while the triangles show rapidly rotating models (rotation period 10 hr). For each rotation period, models with a range of buoyancy fluxes were performed. The dotted and dashed lines show Equations (22) and (23), respectively.

yielding (e.g., Clayton 1968; Stevenson 1979)

$$w \sim \left(\frac{\alpha g F l}{\rho c_p}\right)^{1/3}. \tag{22}$$

In contrast, in a rapidly rotating convective flow, convective buoyancy forces often approximately balance vertical Coriolis forces. Assuming that the turbulent motions are approximately isotropic (i.e., horizontal eddy velocities are comparable to vertical convective velocities), one instead obtains a vertical velocity

$$w \sim \gamma \left(\frac{\alpha g F}{\rho c_p \Omega}\right)^{1/2}, \tag{23}$$

where we have introduced a dimensionless prefactor γ that is expected to be of the order of unity. Laboratory experiments in rotating tanks demonstrate that this expression works well in explaining the convective velocities in the rapidly rotating regime (Golitsyn 1980, 1981; Boubnov & Golitsyn 1990; Fernando et al. 1991). A similar expression has also been suggested for the dynamo-generating region of planetary interiors where a three-way force balance between buoyancy, Coriolis, and Lorentz forces may prevail (Starchenko & Jones 2002; Stevenson 2003, 2010). Showman et al. (2011) showed that it also provides a good match for convective velocities under Jupiter conditions.

Our models demonstrate that under typical brown-dwarf conditions, the rotating scaling (23) provides a significantly better match to the convective velocities than the non-rotating scaling (22). This is illustrated in Figure 3, which shows vertical velocities for our fully equilibrated brown-dwarf models.[10] Symbols depict the mass-weighted, global-mean vertical velocities for a sequence of models that are slowly rotating (circles, rotation period 100 hr) and rapidly rotating (triangles, rotation period 10 hr). They are plotted against the mass-weighted, global-mean buoyancy flux, $\alpha g F/\rho c_p$, for each model.

[10] These and all subsequent models are fully equilibrated brown-dwarf models forced by internally distributed heating and cooling, thereby (unlike Figure 2) avoiding the generation of unrealistic lower thermal boundary layers.

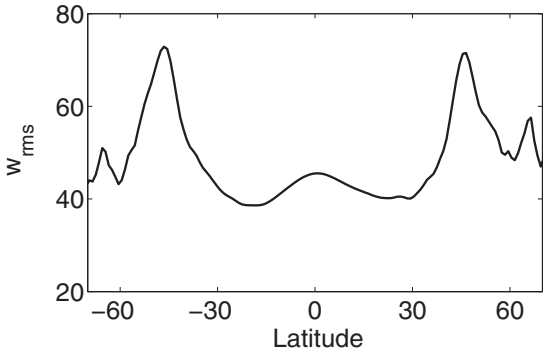

Figure 4. Characteristic vertical convective velocities versus latitude in a convection model with a rotation period of 10 hr, indicating that convective velocities tend to be greater at mid to high latitudes than at low latitudes. Velocities are calculated at a given latitude and pressure as the rms in longitude and time.

There are several points to note in Figure 3. First, the velocities in the rapidly rotating models are smaller than in the slowly rotating models, indicating the rotational suppression of convective motions. Second, the models show that the dependence of vertical velocity on buoyancy flux is weaker in the slowly rotating case than in the rapidly rotating case. The dotted line shows the non-rotating scaling (22), with a mixing length of 816 km, while the dashed line gives the rotating scaling (23), with a prefactor $\gamma = 0.75$. The agreement is good, showing that in our slowly rotating models, the mass-weighted mean vertical velocities scale approximately as buoyancy flux to the one-third power, whereas in our rapidly rotating models, the mass-weighted mean vertical velocities scale approximately as buoyancy flux to the one-half power—just as predicted by Equations (22) and (23), respectively. At a given buoyancy flux, the two scalings shown in Figure 3 differ by only a factor of a few, but the discrepancy becomes greater with decreasing buoyancy flux, and the two predictions differ significantly for conditions inside a typical L/T dwarf. Adopting parameters appropriate for an L/T dwarf ($\alpha \approx 10^{-5}$ K, $c_p \approx 10^4$ J kg^{-1} K^{-1}, and $F \sim 10^4$–10^5 W m^{-2}, corresponding to effective temperatures of ∼650 to 1150 K) yields buoyancy fluxes appropriate to the bulk interior of $\sim 10^{-6}$ to 10^{-5} m^2 s^{-3}. For these values, the convective velocities predicted by the rotating scaling are an order of magnitude lower than those predicted by the non-rotating scaling.

Under conditions appropriate to a typical T dwarf, Equation (23) predicts velocities of ∼0.1 m s^{-1} in the deep interior, ∼10 m s^{-1} at 1000 bar, and ∼40 m s^{-1} at 100 bar. However, the equation likely overpredicts the velocities near the top of the convection zone. In particular, because α/ρ is large near the outer boundary, the buoyancy forces are large, and this likely implies a breakdown of Equation (23) in the outermost part of the convection zone. Interactions of convection with the radiative–convective boundary may also be important in modifying the convective velocities there, an effect not included in Equation (23).

The convective velocities tend to be greater at high latitudes than at low latitudes, as expected from angular momentum constraints. This is illustrated in Figure 4 for a model with a rapid (10 hr) rotation period. Radial convective motion at low latitudes can only occur if fluid parcels gain or lose significant angular momentum as they change distance from the rotation axis; in contrast, convective motion near the poles involves comparatively modest changes in distance from the rotation axis and

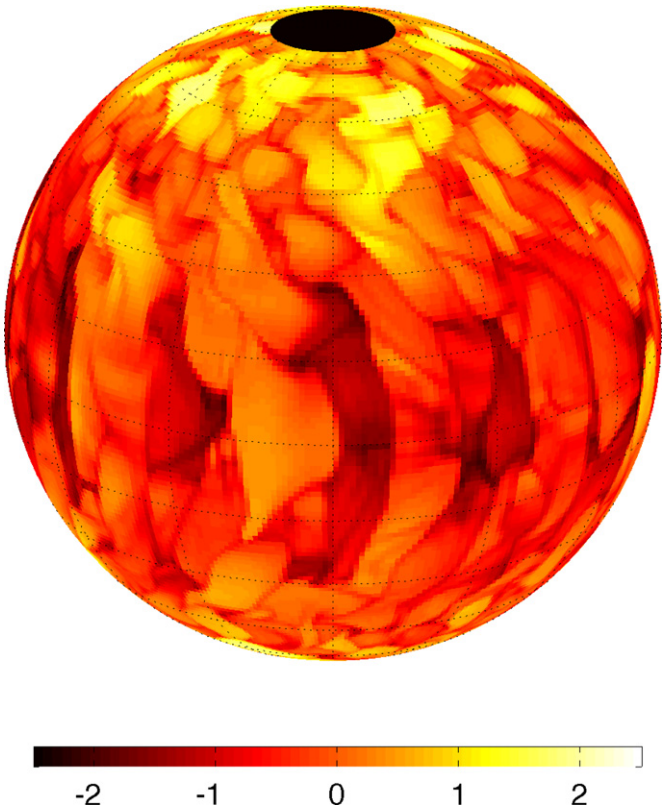

Figure 5. Temperature variations at 1 bar in a typical, rapidly rotating brown-dwarf model. The colorscale gives the temperature perturbation T' at 1 bar, that is, the deviation of temperature from its reference value. Rotation period is 10 hr.
(A color version of this figure is available in the online journal.)

can occur more readily. The result is greater convective velocities near the poles than the equator. Nevertheless, rotational constraints still influence high-latitude convection: the continuity equation demands that the vertical convective motion must necessarily be accompanied by horizontal convergence and divergence and thus motions toward or away from the rotation axis. At large scales, when the Rossby number is small, such rotational constraints will still play an inhibiting role in the efficiency of polar convection. This may explain why the velocities in Figure 4 vary by only a factor of ∼2 from equator to pole.

We now examine the large-scale flow in our fully equilibrated brown-dwarf models. The temperatures develop significant spatial structure at regional-to-global scales, as shown at the 1 bar level in Figure 5 for a typical model. Over a wide range of conditions, the temperatures exhibit significant latitudinal gradients, with polar temperatures exceeding equatorial temperatures by typically a few K. This equator-to-pole temperature difference results from the greater efficiency of convection in polar regions than equatorial regions. Cooling to space continually decreases the entropy of fluid near the ∼1 bar level; in polar regions, this low-entropy fluid readily sinks and is replaced with higher-entropy material rising from below. However, in equatorial regions, the suppression of radial convection inhibits the dense, low-entropy fluid at ∼1 bar from readily sinking. The characteristic hot-poles-cold-equator pattern seen in Figure 5 is the result. We emphasize that this effect emerges naturally from the dynamics and is not the result of any latitudinally varying forcing; indeed, our forcing and boundary conditions are independent of latitude.

The temperature patterns also develop significant variations in both longitude and latitude on regional scales of typically

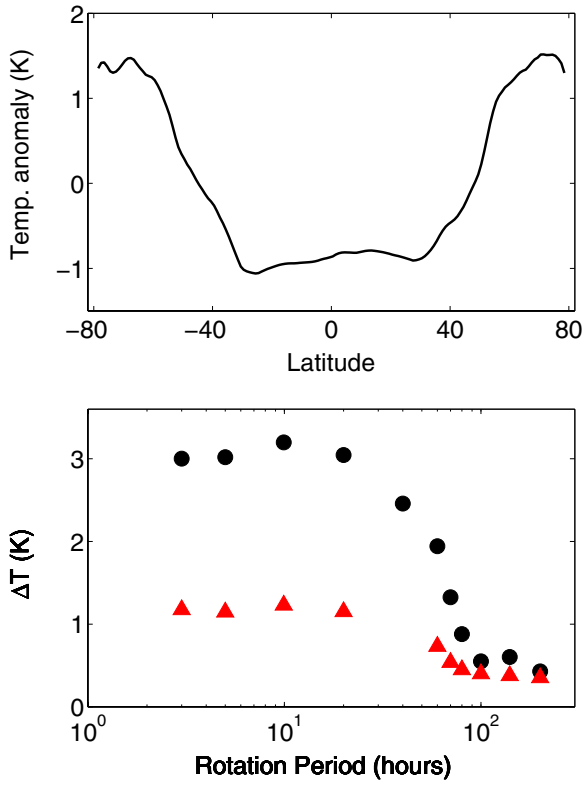

Figure 6. Top: longitudinal-mean temperature vs. latitude at 1 bar for a model with a rotation period of 10 hr, illustrating the emergence of a systematic equator-to-pole temperature difference. Bottom: black dots show longitudinally averaged pole-to-equator temperature differences, and red triangles denote the rms horizontal temperature fluctuations, both at 1 bar, for a sequence of otherwise identical models varying in rotation period from 3 to 200 hr.

(A color version of this figure is available in the online journal.)

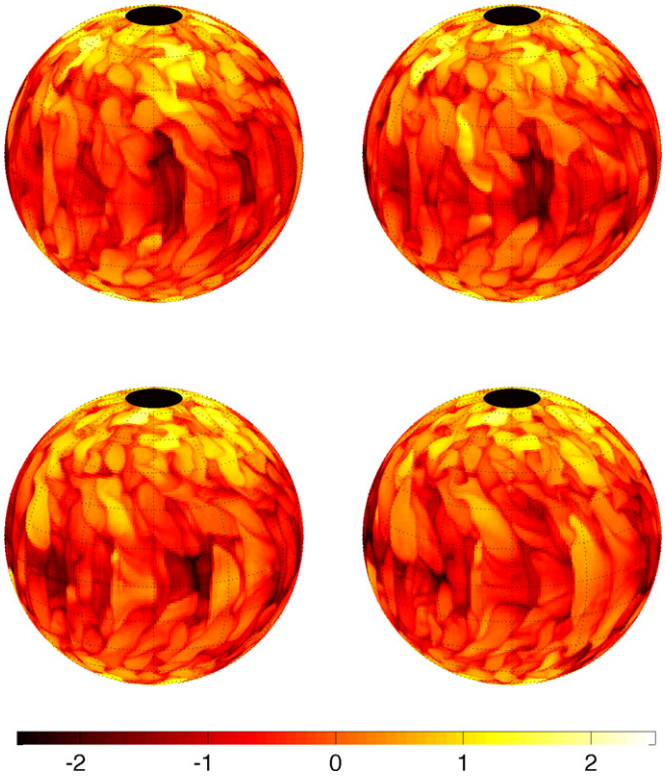

Figure 7. Snapshots at different times of the temperature perturbations at 1 bar in a single model with rotation period of 10 hr. Temperature perturbations are deviations of temperature from the reference state, in K. Time separation between frames is 4.8 hr. The full sequence of model snapshots can be viewed on the authors' Web sites.

(A color version of this figure is available in the online journal.)

$\sim 10^7$ m (Figure 5). Convection produces regional-scale thermal anomalies that vary substantially in time. At high latitudes, these regional anomalies tend to exhibit comparable longitudinal and latitudinal scales, as might be expected from the fact that the plumes move nearly vertically and converge or diverge horizontally in a quasi-isotropic fashion there. At low latitudes, however, the structures exhibit north–south elongation. This is the manifestation of the columnar structure taken by the convection at relatively large scales. Note that real brown dwarfs also likely exhibit short-lived convective structure at very small scales (e.g., granulation) that would be superposed on the larger-scale structure like that shown in Figure 5. Resolving such small-scale structure in global models would require simulations at significantly higher spatial resolution than explored here, which will be a computational challenge for the future.

The characteristic convective temperature perturbations and equator-to-pole temperature differences in our models decrease with increasing rotation period. This is illustrated in Figure 6. The top panel shows the longitudinal (zonal) mean temperature versus latitude at the 1 bar level for a model with a rotation period of 10 hr, illustrating the hot poles and cold equator with a difference of $\sim$2 K. The bottom panel shows the equator-to-pole temperature difference (black circles) and rms temperature variations (red triangles), both at the 1 bar level, for a sequence of models with differing rotation periods. Both the equator-to-pole temperature differences and rms temperature perturbations are nearly constant from rotation periods of 3 hr to $\sim$40 hr. At rotation periods exceeding $\sim$50 hr, however, the temperature perturbations decrease significantly. This results from the fact that at long rotation periods, the Rossby number becomes large and the convection is no longer rotationally inhibited.

The temperature contrasts expected in the convecting region can be understood by combining Equations (21) and (23) to yield a relation for the convective temperature perturbations in a rotationally dominated flow (see Showman et al. 2010)

$$\delta T \sim \left(\frac{F\Omega}{\rho c_p \alpha g}\right)^{1/2}. \quad (24)$$

Our models are performed for Jovian-like internal profiles, corresponding to $\Omega = 1.74 \times 10^{-4}\,\mathrm{s}^{-1}$, $c_p = 1.3 \times 10^4\,\mathrm{J\,kg^{-1}\,K^{-1}}$, and gravity, density, and thermal expansivity at the 1 bar level of $23\,\mathrm{m\,s^{-2}}$, $0.2\,\mathrm{kg\,m^{-3}}$, and $0.006\,\mathrm{K^{-1}}$, respectively. As discussed in detail by Showman et al. (2011), global convective models of giant planets must, for computational reasons, be overforced by several orders of magnitude; our model adopts a heat flux near 1 bar that is close to $10^7\,\mathrm{W\,m^{-2}}$. For these values, Equation (24) predicts $\delta T \sim 2$ K, very similar to the values actually occurring in our models (e.g., Figure 5). This indicates that Equation (24) provides a reasonable representation of the model behavior. Extrapolating now to the conditions of a typical L/T dwarf, we adopt a temperature of 1000 K, corresponding to a radiated IR flux of $F \sim 6 \times 10^4\,\mathrm{W\,m^{-2}}$. Inserting parameters appropriate to the 1 bar level of a brown dwarf ($\rho = 0.03\,\mathrm{kg\,m^{-2}}$, $c_p = 1.3 \times 10^4\,\mathrm{J\,kg^{-1}\,K^{-1}}$, $\alpha = 10^{-3}\,\mathrm{K}$, $\Omega = 3 \times 10^{-4}\,\mathrm{s^{-1}}$, and $g = 200\,\mathrm{m\,s^{-2}}$), we obtain $\delta T \sim 0.5$ K as the expected convective temperature perturbation for a typical brown dwarf.

The convective structure exhibits significant temporal variability, as can be seen in Figure 7. The figure shows the 1 bar temperature structure (at the top of the convection zone) at 4.8 hr

intervals in a brown-dwarf model with a rotation period of 10 hr. Such convective variability should cause significant variability in the overlying atmosphere, helping to explain the variability in light-curve shapes observed in several L/T dwarfs (Artigau et al. 2009; Radigan et al. 2012). We return to the dynamics of the stratified atmosphere in Section 4.

3.3. Large-scale Flow Organization in the Convection Zone

Here we address the question of whether or not the convection zone can develop organized, large-scale horizontal winds such as fast east–west (zonal) jets, since these might play a role in causing differential zonal motion of cloudy and cloud-free regions in the overlying atmosphere.

At pressures $\gtrsim$1 Mbar, hydrogen metallizes and magnetohydrodynamic (MHD) effects become important (e.g., Weir et al. 1996; Nellis et al. 1995, 1996; Nellis 2000, 2006). Theoretical arguments and numerical simulations of convection in electrically conducting spherical shells—as applied to Jupiter, Earth's outer core, and related systems—suggest that the Lorentz force acts to brake the large-scale east–west (zonal) winds when the electrical conductivity is high, inhibiting jet formation in the metallic region (e.g., Kirk & Stevenson 1987; Grote et al. 2000; Busse 2002; Liu et al. 2008). Numerical simulations of dynamo generation in convecting, rotating fluids at high electrical conductivity have led to scaling laws for the magnetic field strength of rapidly rotating planets and convective stars (Christensen & Aubert 2006; Christensen et al. 2009; Christensen 2010). Application of these scaling laws to brown dwarfs predicts that brown dwarfs will exhibit strong magnetic fields (Reiners & Christensen 2010). These dynamo experiments also lead to scaling laws for the mean flow velocities in the dynamo-generating region (Christensen & Aubert 2006; Christensen 2010). When heat fluxes, rotation rates, and densities appropriate to typical L/T-transition dwarfs are adopted ($F \sim 10^5\,\mathrm{W\,m^{-2}}$, $\Omega \sim 10^{-3}$–$10^{-4}\,\mathrm{s^{-1}}$, and $\rho \sim 1$–$5 \times 10^4\,\mathrm{kg\,m^{-3}}$), these scaling laws predict typical fluid velocities of $\sim$0.1–0.3 $\mathrm{m\,s^{-1}}$—similar to estimates from Equation (23) under the same assumptions. Overall, these results suggest that the flow speeds are weak in the metallic interiors of brown dwarfs. We for now proceed under the assumption that the large-scale horizontal winds are weak in the metallic region, and ask what happens in the overlying molecular envelope.

The emergence of large-scale, organized horizontal temperature gradients (see Figures 5 and 6) implies that the flow will develop large-scale shear of the zonal wind in the direction along the rotation axis via the thermal-wind equation (7). We here write this in the form

$$2\Omega \frac{\partial u}{\partial \hat{z}} \approx g k_{\rm jet} \frac{\delta\rho}{\rho} \approx g k_{\rm jet} \alpha \delta T, \qquad (25)$$

where $\delta\rho$ and δT are the characteristic large-scale horizontal density and temperature differences (on isobars) which occur over a horizontal wavenumber $k_{\rm jet}$ (between the equator and pole, for example). We envision that these horizontal density and temperature differences result from large-scale organization of the convective temperature fluctuations, and we therefore equate δT in Equation (25) to that from Equation (24). Doing so yields a characteristic variation of the zonal wind along $\hat{z}$ of

$$\Delta u \approx \frac{k_{\rm jet}}{2} \int \left(\frac{F g \alpha}{\rho c_p \Omega} \right)^{1/2} d\hat{z}. \qquad (26)$$

The quantity α/ρ in the integrand of Equation (26) varies by orders of magnitude from the atmosphere to the deep interior and must be accounted for. In contrast, F, g, and c_p vary radially by a factor of two or less across the molecular envelope (see Kaspi et al. 2009), and to a first approximation—here seeking simply an order-of-magnitude expression—we can treat them as constant. If we furthermore adopt the ideal-gas EOS, which is reasonably accurate in the outermost layers, and assume that the background thermal profile is an adiabat, we can integrate Equation (26) analytically to obtain the characteristic difference in zonal wind (along $\hat{z}$) between a deep pressure $p_{\rm bot}$ and some low pressure p:

$$\Delta u \approx \frac{-R k_{\rm jet} \theta}{(1-2\kappa)|\sin\phi| p_0^{\kappa}} \left(\frac{FR}{c_p g \Omega} \right)^{1/2} \left[\frac{1}{p^{\frac{1}{2}-\kappa}} - \frac{1}{p_{\rm bot}^{\frac{1}{2}-\kappa}} \right], \qquad (27)$$

where we have used the fact that the pressure variation along $\hat{z}$ is overwhelmingly dominated by the hydrostatic contribution. In Equation (27), $\theta = T(p_0/p)^{\kappa}$ is the potential temperature of the adiabat (that is, a representation of the entropy of the adiabat), p_0 is a reference pressure (which we take here to be 1 bar), R is the specific gas constant, $\kappa = R/c_p$, and the region under consideration has a characteristic latitude ϕ.

Adopting values appropriate to a typical brown dwarf ($R = 3700\,\mathrm{J\,kg^{-1}\,K^{-1}}, \kappa = 2/7, \theta = 1000\,\mathrm{K}, \Omega \approx 3 \times 10^{-4}\,\mathrm{s^{-1}}, \phi \approx 30^{\circ}$, $F \sim 10^5\,\mathrm{W\,m^{-2}}$, $g \approx 500\,\mathrm{m\,s^{-2}}$, and $k_{\rm jet} = 1 \times 10^{-7}\,\mathrm{m}$ corresponding to a wavelength of approximately one Jupiter radius), the equation can be expressed as

$$\Delta u \approx 2 \left[\left(\frac{1\,\mathrm{bar}}{p} \right)^{\frac{1}{2}-\kappa} - \left(\frac{1\,\mathrm{bar}}{p_{\rm bot}} \right)^{\frac{1}{2}-\kappa} \right] \mathrm{m\,s^{-1}}. \qquad (28)$$

We are interested in the wind shear between the deep interior and the top of the convection zone, where the pressure is approximately $p \sim 1$ bar. Interestingly, when we consider any deep pressure $p_{\rm bot} \gg p$, the second term in Equation (28) drops out and the equation becomes independent of $p_{\rm bot}$; this is because the factor α/ρ becomes extremely small at high pressure, so that almost all of the contribution to Δu comes from the outermost few scale heights of the convection zone—even if a very deep layer is being considered. With the adopted parameters, we then obtain $\Delta u \sim 2\,\mathrm{m\,s^{-1}}$ for the difference in zonal wind (in the direction of $\hat{z}$) between any deep level and 1 bar. The implication is that given the expected temperature variations associated with convection, the large-scale wind varies by at most a few $\mathrm{m\,s^{-1}}$ along the direction of the rotation axis. If the large-scale, zonal-mean horizontal wind is weak in the deep interior where MHD effects predominate, then it will also be weak near the top of the convection zone. If, rather than adopting a horizontal length scale $2\pi/k_{\rm jet}$ of a Jupiter radius, we instead adopt a smaller length scale (e.g., 0.1 Jupiter radius, appropriate to the regional-scale temperature anomalies seen in Figure 5), we then conclude that horizontal winds of tens of $\mathrm{m\,s^{-1}}$ are possible at the top of the convection zone. Despite the uncertainties, these estimates suggest that the large-scale zonal and meridional wind speeds in the convection zone are $<10^2\,\mathrm{m\,s^{-1}}$ for typical brown dwarfs.

4. DYNAMICS OF THE STRATIFIED ATMOSPHERE

We have so far emphasized the convective interior, but infrared spectra and light curves emerge from pressures that for a wide range of effective temperature lie within the stratified atmosphere overlying the convective region (e.g., Burrows et al. 2006a). Understanding this stratified region is therefore crucial

for understanding observations. In particular, the horizontal temperature differences, wind speeds, and dominant flow length scales in this layer will control the variability in IR light-curves, and vertical mixing rates will control cloudiness and chemical disequilibrium. Here we outline the expected dynamics of this stratified layer.

4.1. Qualitative Mechanism of Atmospheric Circulation

At first glance, it is not obvious that brown dwarfs should exhibit significant large-scale circulations in their atmospheres. Because they receive no external irradiation, the temperature–pressure profiles in their stratified atmospheres are determined primarily by absorption of upwelling IR radiation from below. Since the interior entropy of a brown dwarf varies little with latitude, one might therefore expect that the radiative-equilibrium temperature profile of the stratified atmosphere should vary little with latitude, and that—at least at large scales—the stratified regions will be relatively quiescent. This contrasts significantly from the tropospheres of most solar-system planets—and hot Jupiters—where differential stellar heating between equator and pole (or day and night) leads to a thermally driven atmospheric circulation.

However, the interaction of convective turbulence with the stable layer on brown dwarfs will perturb the stratified layer and generate a wide spectrum of atmospheric waves, including gravity waves (e.g., Goldreich & Kumar 1990; Freytag et al. 2010) and Rossby waves. In solar-system atmospheres, including those of Earth, Jupiter, Saturn, Uranus, and Neptune, such waves generated in the troposphere by convection and various instabilities propagate upward into the stratosphere. The interaction of these waves with the mean flow—in particular, the generation, absorption, breaking, and dissipation of these waves—induces a large-scale circulation in the stratosphere. Indeed, despite the existence of equator-to-pole radiative (thermal) forcing in irradiated atmospheres, this *mechanical*, wave-induced forcing is perhaps the dominant driver of the stratospheric circulation on the Earth and the giant planets (for reviews, see, e.g., Andrews et al. 1987; Shepherd 2000, 2003; Haynes 2005). In a similar way, we envision that the breaking, absorption, and dissipation of convectively generated waves will drive a large-scale circulation in the stratified atmospheres of brown dwarfs.

A variety of nonlinear interactions and feedbacks enhance the ability of such wave/mean-flow interactions to drive an atmospheric circulation. For example, vertically propagating waves are preferentially absorbed near critical layers where the background flow speed matches the wave speed; such absorption causes an acceleration of the mean flow that is spatially coherent. In Earth's atmosphere, this effect allows convectively generated waves propagating upward from the troposphere to drive zonal jets in the stratosphere, a phenomenon known as the "quasi-biennial oscillation" or QBO (Baldwin et al. 2001). A similar phenomenon has been observed on Jupiter (Friedson 1999) and has been suggested to occur in hot stars (e.g., Rogers et al. 2012). Likewise, the mixing induced by breaking Rossby waves is spatially inhomogeneous and naturally leads to the formation of jets and vortices (e.g., Dritschel & McIntyre 2008). Idealized numerical experiments of two-dimensional and stratified, 3D, rapidly rotating flows demonstrate that random turbulent forcing can generically lead to the generation of large-scale vortices and jets (e.g., Nozawa & Yoden 1997; Huang & Robinson 1998; Marcus et al. 2000; Smith & Vallis 2001; Smith 2004; Scott & Polvani 2007; Showman 2007; Dritschel & McIntyre 2008; Dritschel & Scott 2011).

Regardless of the details of this forcing, the rapid rotation will dominate the physical structure of such a circulation at large scales (defined here as, say, $\gtrsim 10^3$ km). The small Rossby numbers expected at large scales imply that this circulation will be geostrophically balanced, that is, pressure-gradient forces will approximately balance Coriolis forces in the horizontal momentum equation. Here, we adopt the primitive equations, which are the standard equations governing atmospheric flows in stably stratified atmospheres when the horizontal dimensions greatly exceed the vertical dimensions (for reviews, see Pedlosky 1987; Vallis 2006; Showman et al. 2010). Using log pressure as a vertical coordinate, geostrophy reads

$$fu = -\left(\frac{\partial \Phi}{\partial y}\right)_p, \quad fv = \left(\frac{\partial \Phi}{\partial x}\right)_p, \tag{29}$$

where u and v are the east–west (zonal) and north–south (meridional) wind on isobars, Φ is the gravitational potential on isobars, x and y are eastward and northward distance, respectively, and the derivatives are taken on constant-pressure surfaces. Here, $f \equiv 2\Omega \sin\phi$ is the Coriolis parameter. When combined with local hydrostatic balance—valid in the stratified atmosphere at horizontal scales greatly exceeding vertical ones—geostrophy implies that the vertical shears of the horizontal wind relate to the horizontal temperature gradients via the thermal-wind equation (e.g., Pedlosky 1987; Vallis 2006)

$$f\frac{\partial u}{\partial \tilde{z}} = -R\frac{\partial T}{\partial y}, \quad f\frac{\partial v}{\partial \tilde{z}} = R\frac{\partial T}{\partial x}, \tag{30}$$

where $\tilde{z} \equiv -\ln p$ is the vertical coordinate. At large scales, then, the development of fast winds in the atmosphere—particularly if the large-scale winds in the convection zone are weak—depends on the ability of the atmosphere to maintain horizontal temperature gradients.

What is the nature of this wave-driven circulation? Figure 8 provides a schematic illustration of the dynamics. Generally, the acceleration of large-scale horizontal winds by waves or turbulence induces deviations from geostrophy, leading to a mismatch between the pressure-gradient and Coriolis forces in the direction perpendicular to the wind. This unbalanced force drives a so-called secondary circulation in the plane perpendicular to the main geostrophic flow; the Coriolis forces and entropy advection caused by this circulation act to restore geostrophy. This standard mechanism is well understood (see Haynes et al. 1991 for theory, and James 1994, pp. 100–107, or Holton 2004, pp. 313–327, for brief reviews) and provides the dynamical link between the horizontal winds, temperature perturbations, and vertical velocities.

4.2. Quantitative Model of Atmospheric Circulation

Although the amplitude of the wave driving in brown-dwarf atmospheres remains unknown, the above dynamical arguments allow us to determine the relationship between the horizontal winds, temperature contrasts, and vertical velocities *as a function* of the wave-driving amplitude. We here construct a simple analytic theory of this atmospheric circulation, treating the wave-driving amplitude as a free parameter. The model is approximate and makes a number of simplifying assumptions in the spirit of exposing the dynamics in the simplest possible context. As a result, the model is not expected to be accurate in quantitative detail. Rather, the goal is to broadly illustrate

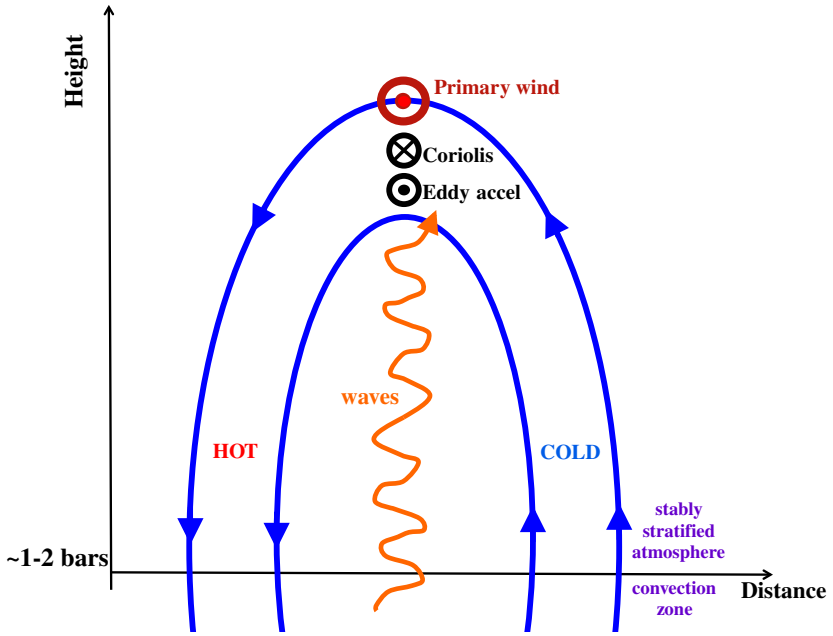

Figure 8. Schematic illustration of a wave-driven atmospheric circulation, as occurs in the stratospheres of Earth, Jupiter, Saturn, Uranus, and Neptune and as we propose occurs at regional-to-global scales in the stably stratified atmospheres of brown dwarfs. Gravity and Rossby waves (orange) propagate from the convective zone into the atmosphere, where they break or dissipate and induce an acceleration of the mean wind, here illustrated as a vector coming out of the page (black ⊙ symbol labeled "eddy accel"). This drives a horizontal wind here also represented as a vector coming out of the page (red ⊙ symbol labeled "primary wind"). The resulting deviation from geostrophy drives a weak secondary circulation (blue contours) in the plane perpendicular to the primary wind. In steady state, the eddy acceleration is balanced by a Coriolis acceleration (⊗ symbol, representing a vector pointing into the page) associated with the secondary circulation. Vertical motion associated with the secondary circulation advects entropy vertically, leading to horizontal temperature contrasts (labeled "hot" and "cold"). These temperature contrasts are precisely those needed to maintain thermal-wind balance with the vertical shear of the primary wind. Scales are uncertain but are plausibly thousands to tens of thousands of kilometers horizontally and several scale heights vertically.

(A color version of this figure is available in the online journal.)

the types of physical processes governing the atmospheric circulation on brown dwarfs, and to obtain order-of-magnitude estimates for the horizontal temperature perturbations and wind speeds, quantities important in shaping the observables.

In steady state, the momentum balance in the direction parallel to the geostrophic wind reads, to order of magnitude,[11]

$$f\overline{v} \sim \mathcal{A}, \tag{33}$$

where $\overline{v}$ is the horizontal flow perpendicular to the main geostrophic flow and $\mathcal{A}$ is the characteristic magnitude of the eddy-induced acceleration of the mean flow, due to braking, absorption, or dissipation of gravity or Rossby waves. What this equation implies is that the wave interactions with the mean flow drive a so-called secondary circulation, $\overline{v}$ (meridional in the case of zonal jets, radially toward or away from the vortex center in the case of a large vortex). See Figure 8 for the conceptual picture.

The associated vertical velocity can be obtained from the continuity equation, which for the primitive equations in log-pressure coordinates reads

$$\frac{\partial \overline{v}}{\partial y} + e^{\tilde{z}} \frac{\partial}{\partial \tilde{z}}(e^{-\tilde{z}}\overline{\varpi}) = 0, \tag{34}$$

which we can approximate to order of magnitude as

$$\overline{v}l \sim \frac{\overline{\varpi}}{\Delta\tilde{z}}, \tag{35}$$

where $\overline{\varpi}$ is the characteristic vertical velocity (in units of scale heights per sec), $\Delta\tilde{z}$ is the vertical scale of the circulation (in units of scale heights), and l is the dominant horizontal wavenumber of the circulation. Equations (33) and (35) imply that

$$\overline{\varpi} \sim \overline{v}l\Delta\tilde{z} \sim \frac{l\mathcal{A}\Delta\tilde{z}}{f}. \tag{36}$$

Thus, wave interactions with the mean flow drive large-scale vertical motions.

[11] Suppose, for concreteness, that the dominant geostrophic flow consists of zonal jets, as exist on Jupiter. The significant zonal symmetry of such jets suggests decomposing the flow into zonal-mean and deviation (eddy) components, $A = \overline{A} + A'$. By expanding the zonal momentum equation and zonally averaging, we obtain the Eulerian-mean equation for the evolution of the zonal-mean flow, $\overline{u}$, over time (adopting Cartesian geometry for simplicity)

$$\frac{\partial \overline{u}}{\partial t} = -\overline{v}\frac{\partial \overline{u}}{\partial y} - \overline{\varpi}\frac{\partial \overline{u}}{\partial \tilde{z}} + f\overline{v} - \frac{\partial(\overline{u'v'})}{\partial y} - e^{\tilde{z}}\frac{\partial(e^{-\tilde{z}}\overline{u'\varpi'})}{\partial \tilde{z}}, \tag{31}$$

where $\varpi = d\tilde{z}/dt = -d\ln p/dt$ is the vertical velocity in log-pressure coordinates. Thus, the absorption, breaking, or dissipation of waves can drive a mean flow, $\overline{u}$. Scaling analysis of this equation immediately shows that on the right-hand side, the first and second terms are both of the order of Ro smaller than the third term. In steady state, then, the balance in a geostrophic flow is between the eddy-driven accelerations and the Coriolis force associated with a mean-meridional circulation, i.e.,

$$f\overline{v} \approx \frac{\partial(\overline{u'v'})}{\partial y} + \frac{\partial(\overline{u'\varpi'})}{\partial \tilde{z}}. \tag{32}$$

If the flow consists predominantly of large vortices rather than zonal jets, one can alternately adopt a cylindrical coordinate system centered on a vortex, where u is the azimuthal flow around the vortex, v is the radial velocity (toward/away from the vortex center), and the eddy-mean-flow composition denotes an *azimuthal* mean around the vortex (overbars) and deviations therefrom (primes). Azimuthally averaging the azimuthal momentum equation then leads to relationships analogous to Equations (31) and (32). In either case, the equation can be expressed, to order of magnitude, as Equation (33).

These wave-driven, large-scale vertical motions will advect entropy vertically, leading to the existence of horizontal temperature variations on isobars. These are in fact exactly the temperature differences needed to maintain the wave-driven geostrophic flow in thermal-wind balance. To quantify, consider the thermodynamic energy equation, which can be expressed as

$$\frac{\partial T}{\partial t} + \mathbf{v}_h \cdot \nabla_h T - \varpi \frac{H^2 N^2}{R} = \frac{q}{c_p}, \quad (37)$$

where T is temperature, $\mathbf{v}_h$ the horizontal velocity, ∇_h the horizontal gradient operator, H the scale height, N the Brunt–Vaisala frequency, q the specific heating rate, and c_p the specific heat. In a statistical steady state, we envision a primary balance between the radiative heating/cooling (right-hand side) and vertical advection (right term on left-hand side). If isentrope slopes are sufficiently large, the horizontal mixing may also contribute via the term $\mathbf{v} \cdot \nabla T$. We write this balance as

$$-\varpi \frac{H^2 N^2}{R} = \frac{q}{c_p} - \mathbf{v}_h \cdot \nabla_h T. \quad (38)$$

We parameterize radiative heating/cooling as Newtonian relaxation of the temperature toward the radiative-equilibrium state, expressed as $q/c_p = (T_{\rm eq} - T)/\tau_{\rm rad}$, where $T_{\rm eq}(\tilde{z})$ is the radiative-equilibrium temperature profile and $\tau_{\rm rad}$ is a specified radiative time constant. Since brown dwarfs receive no external irradiation, $T_{\rm eq}$ is to zeroth order independent of latitude and longitude. To order of magnitude, the characteristic deviation of temperature from its local radiative equilibrium, $T(\tilde{z}) - T_{\rm eq}(\tilde{z})$, is comparable to the characteristic horizontal temperature difference on isobars, $\Delta T_{\rm horiz}$. We also parameterize the meridional eddy mixing as a diffusive process, with eddy diffusivity D. To order of magnitude, we thus have

$$\overline{\varpi} \frac{H^2 N^2}{R} = \frac{\Delta T_{\rm horiz}}{\tau_{\rm rad}} + D l^2 \Delta T_{\rm horiz}. \quad (39)$$

The physical interpretation is that vertical advection (left side) attempts to *increase* the horizontal temperature contrasts, whereas radiation and meridional eddy mixing (right side) both attempt to *decrease* the horizontal temperature contrasts. Here, $\overline{\varpi}$ and $\Delta T_{\rm horiz}$ refer to characteristic magnitudes and are defined positive. Importantly, the two terms on the right-hand side have the same sign, since they both act in the same direction, namely, to damp temperature differences.[12]

Substituting Equation (36) into Equation (39) yields

$$\frac{l \mathcal{A} \Delta\tilde{z} H^2 N^2}{f R} \sim \Delta T_{\rm horiz} \left(\frac{1}{\tau_{\rm rad}} + D l^2 \right), \quad (40)$$

which can readily be solved to yield an expression for the meridional temperature difference in terms of "known" parameters:

$$\Delta T_{\rm horiz} \sim \frac{l \mathcal{A} \Delta\tilde{z} H^2 N^2}{f R \left(\frac{1}{\tau_{\rm rad}} + D l^2 \right)}. \quad (41)$$

[12] Breaking gravity waves will cause a vertical mixing that might be represented as a *vertical* diffusion of entropy, leading to an additional source term in Equation (39). Only horizontal *variations* in the amplitude of this mixing will act to alter $\Delta T_{\rm horiz}$. A priori, it is not clear how such variations will correlate with the overturning circulation nor how to parameterize them in the context of Equation (39). Since our goal is to describe the dynamics of the wave-driven circulation in the simplest possible context, we therefore forgo any inclusion of this vertical mixing term here, with the understanding that more realistic models of the large-scale circulation will probably have to account for it.

We have yet to use the meridional momentum balance (or radial momentum balance in the case of a vortex), and doing so will allow us to solve for the zonal wind several scale heights above the radiative–convective boundary. To order of magnitude, the thermal-wind equation implies

$$\Delta u \sim \frac{R l \Delta T_{\rm horiz} \Delta\tilde{z}}{f}, \quad (42)$$

where Δu is the characteristic difference between the wind speed at the radiative–convective boundary and some level of interest, say, at the mean IR photosphere. If the former is small as suggested in Section 3.3, Δu would approximately give the actual wind speed at levels above the radiative–convective boundary. Inserting Equation (41) into Equation (42), we obtain

$$\Delta u \sim \frac{l^2 \mathcal{A} \Delta\tilde{z}^2 H^2 N^2}{f^2 \left(\frac{1}{\tau_{\rm rad}} + D l^2 \right)}. \quad (43)$$

Together, Equations (36), (41), and (43) provide the expressions we seek for the vertical velocities, horizontal temperature differences, and horizontal wind speeds as a function of $\mathcal{A}$, l, and parameters that are either known or can be estimated. The Coriolis parameter, f, follows directly from the rotation period. For a brown dwarf of a given effective temperature and gravity, 1D radiative-transfer models allow estimates of the vertical temperature–pressure profile (e.g., Marley et al. 1996, 2002, 2010; Burrows et al. 1997, 2006b), and hence HN. Since the infrared photosphere is typically 1–3 scale heights above the radiative–convective boundary (Burrows et al. 2006b), values of $\Delta\tilde{z} \sim$ 1–3 are most appropriate.

What sets the dominant horizontal length scale of the flow, represented in the above theory by the wavenumber l? One possibility is the Rhines scale, given by $(\Delta u/\beta)^{1/2}$, where β is the derivative of the Coriolis parameter with northward distance y. This is generally the scale at which Rossby waves impose anisotropy on the flow, and in many systems, it is the energy-containing scale. The Rhines scale controls the jet widths on Jupiter, Saturn, Uranus, and Neptune (e.g., Cho & Polvani 1996), as well as in a wide range of numerical simulations of stratified, rotating turbulence (for a review, see Vasavada & Showman 2005). For typical brown-dwarf rotation rates and the wind speeds estimated in Figure 9, this yields $l \sim (3\text{–}6) \times 10^{-7}$ m^{-1}, corresponding to horizontal wavelengths of 10,000–20,000 km. Another possibility is that l results from an interaction of turbulent energy transfers with the strong radiative and/or frictional damping. Stratified flows forced at small scales tend to exhibit upscale energy cascades, and a competition between the rate of upscale energy transfer and the radiative damping timescale then determines the dominant length scale. This possibility is at present difficult to quantify. Given the uncertainties, we simply adopt plausible values for l here and leave a detailed investigation for future work.

It is also worthwhile expressing our solutions in terms of the power exerted by the waves in driving the large-scale circulation. The characteristic power per mass exerted by the waves in driving the large-scale circulation is approximately $\mathcal{A}\Delta u$, and the power per unit horizontal area is $\mathcal{A} p \Delta u/g$, where p is the pressure at the radiative–convective boundary. Defining a dimensionless efficiency η, corresponding to the fraction of the brown-dwarf heat flux that is used to drive the atmospheric circulation, we then have $\eta F \sim \mathcal{A} p \Delta u/g$, where F is the heat flux radiated by the brown dwarf. Using this constraint, the

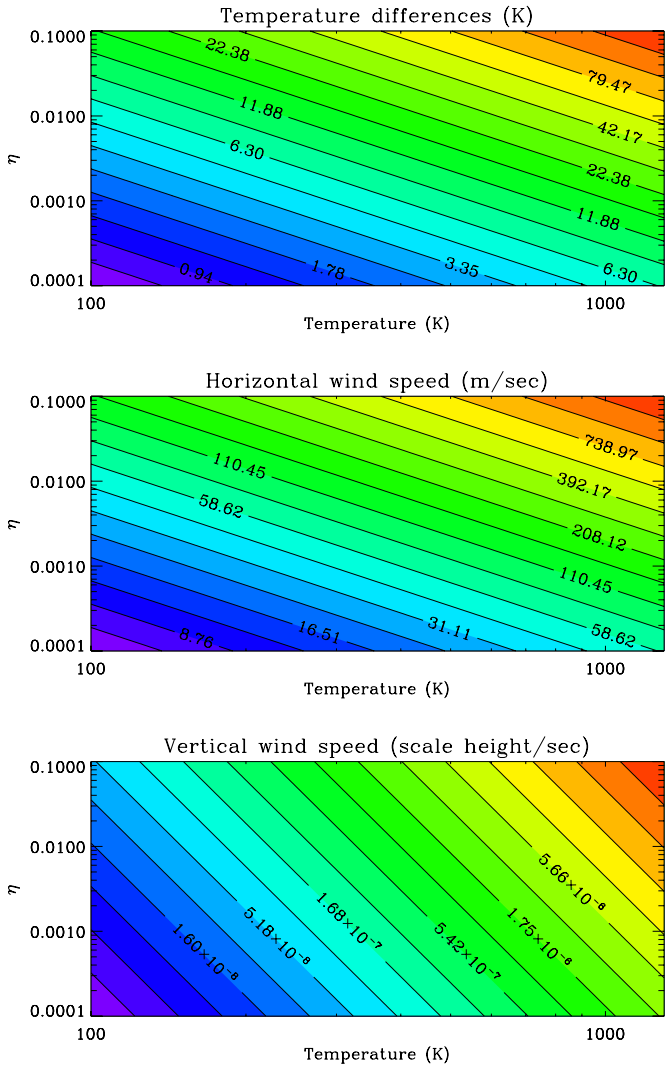

Figure 9. Characteristic horizontal temperature differences (top), horizontal wind speeds (middle), and vertical velocities (bottom) from our solutions for large-scale, wave-driven circulation in the stratified atmosphere, plotted as a function of temperature and dimensionless efficiency by which the waves drive the atmospheric circulation. Plotted values adopt a horizontal wavenumber $l = 6 \times 10^{-7}\,\mathrm{m}^{-1}$ (corresponding to a horizontal wavelength of 10^4 km) and an isothermal vertical background temperature profile (for which $NH = R\sqrt{T/c_p}$). Other parameter values are $R = 3700\,\mathrm{J\,kg^{-1}\,K^{-1}}$, $\Delta\tilde{z} = 2$ (implying a circulation two scale heights tall), and $f = 5 \times 10^{-4}\,\mathrm{s}^{-1}$ (corresponding to a rotation period of five hours).

(A color version of this figure is available in the online journal.)

solutions become

$$\Delta T_{\mathrm{horiz}} \sim \left(\frac{\eta g F}{p}\right)^{1/2} \frac{HN}{R\left(\frac{1}{\tau_{\mathrm{rad}}} + Dl^2\right)^{1/2}}, \tag{44}$$

$$\Delta u \sim \left(\frac{\eta g F}{p}\right)^{1/2} \frac{l\Delta\tilde{z}HN}{f\left(\frac{1}{\tau_{\mathrm{rad}}} + Dl^2\right)^{1/2}}, \tag{45}$$

and

$$\varpi \sim \left(\frac{\eta g F}{p}\right)^{1/2} \frac{1}{HN}\left(\frac{1}{\tau_{\mathrm{rad}}} + Dl^2\right)^{1/2}. \tag{46}$$

If we adopt a blackbody flux, $F = \sigma T^4$, where T is the typical photospheric temperature and σ is the Stefan–Boltzmann constant, and express the radiative time constant as (Showman & Guillot 2002)

$$\tau_{\mathrm{rad}} \sim \frac{pc_p}{4g\sigma T^3}, \tag{47}$$

then Equations (44), (45), and (46) can be expressed as functions of temperature and dimensionless wave-driving efficiency (here for simplicity neglecting the horizontal diffusion term),

$$\Delta T_{\mathrm{horiz}} \sim \left(\frac{\eta c_p T}{4}\right)^{1/2} \frac{NH}{R}, \tag{48}$$

$$\Delta u \sim \left(\frac{\eta T c_p}{4}\right)^{1/2} \frac{l\Delta\tilde{z}HN}{f}, \tag{49}$$

and

$$\varpi \sim \frac{2\eta^{1/2} g T^{7/2}\sigma}{c_p^{1/2} pHN} \sim \frac{2(\eta T c_p)^{1/2}}{HN\tau_{\mathrm{rad}}}. \tag{50}$$

Noting that HN is the approximate horizontal phase speed of long-vertical-wavelength gravity waves, inspection of Equations (48)–(50) makes clear that to within factors of the order of unity,

1. $\Delta T_{\mathrm{horiz}}/T$ is $\eta^{1/2}$ times the ratio of the gravity wave speed to the sound speed,
2. Δu over the sound speed is $\eta^{1/2}$ times the ratio of the Rossby deformation radius, $L_D = \Delta\tilde{z}HN/f$, to the dominant horizontal length scale of the flow, and
3. ϖ is $\eta^{1/2}\tau_{\mathrm{rad}}^{-1}$ times the ratio of the sound speed to the gravity wave speed (in other words, the time for the flow to advect vertically over a scale height is $\eta^{-1/2}\tau_{\mathrm{rad}}$ times the ratio of the gravity wave speed to the sound speed).

For an isothermal, ideal-gas atmosphere, $HN = R\sqrt{T/c_p}$, and the ratio of HN to the sound speed is $\sqrt{\kappa(1-\kappa)}$, which is ~0.4 for an H_2 atmosphere with $\kappa = 2/7$. Thus, the ratio of the gravity wave speed to the sound speed is of the order of unity. These arguments imply that for small wave-driving efficiencies ($\eta \ll 1$), the fractional horizontal temperature differences will be small, the horizontal wind speeds will be much less than the sound speed, and the time for air to advect vertically over a scale height will be much longer than the radiative time constant.

4.3. Application of the Theory to Giant Planets and Brown Dwarfs

Detailed numerical simulations of convection impinging on a stable layer will be necessary to quantify the value of η, but several previous studies provide constraints. In a theoretical investigation of convection interacting with an overlying isothermal radiative zone, Goldreich & Kumar (1990) found that the fraction of the convective heat flux converted into gravity waves is approximately the Mach number associated with the convection, which may be ~0.01 for typical brown dwarfs. This presumably provides an upper limit on η since only a fraction of the energy converted to waves is actually used to drive a large-scale circulation. Rough estimates for the Earth's stratosphere[13] indicate

[13] In Earth's mid and high latitudes, upwardly propagating waves lead to typical accelerations of the zonal-mean zonal wind of the order of $\mathcal{A} \sim 10^{-5}\,\mathrm{m\,s^{-2}}$ in the stratosphere (Andrews et al. 1987; Vallis 2006, Chapter 13). Typical zonal wind speeds in these regions are $\Delta u \sim 20\,\mathrm{m\,s^{-1}}$. Adopting a pressure $p \sim 0.1$ bar representative of the lower stratosphere, this implies a power per area driving stratospheric motions of $\mathcal{A}p\Delta u/g \sim 0.2\,\mathrm{W\,m^{-2}}$. Since Earth's global-mean radiated flux is $F = 240\,\mathrm{W\,m^{-2}}$, the implied efficiency is $\eta \sim \mathcal{A}p\Delta u/(Fg) \sim 10^{-3}$. For Jupiter, observational diagnosis of stratospheric heating patterns implies typical eddy accelerations of the zonal-mean zonal wind exceeding $\mathcal{A} \sim 10^{-6}\,\mathrm{m\,s^{-2}}$ in the lower stratosphere (West et al. 1992; Moreno & Sedano 1997). Given a typical stratospheric wind speed of ~20 m s^{-1}, lower stratospheric pressure of 0.1 bar, and a radiated flux of $F \sim 14\,\mathrm{W\,m^{-2}}$, this again implies an efficiency $\eta \sim 10^{-3}$.

that waves drive a circulation with an efficiency $\eta \sim 10^{-3}$. Information is limited for Jupiter but likewise suggests $\eta \sim 10^{-3}$ (footnote 13). While future work is clearly needed, these estimates suggest that values of η ranging from 10^{-4} to 10^{-2} may be appropriate for brown dwarfs.

We first test the theory on Jupiter's stratospheric circulation. Jupiter's mean stratospheric temperature profile rises from the ~110 K tropopause minimum at 150 mbar to ~170 K at 1 mbar pressure. *Voyager* and *Cassini* observations show that, throughout this pressure range, the temperature and zonal wind vary on characteristic horizontal (meridional) scales of $\sim 10^4$ km. On these scales, temperatures vary by ~3–5 K at most latitudes, reaching 10 K at a few latitudes and pressures (Simon-Miller et al. 2006). Analysis of these observations indicates that from 1 to 100 mbar, zonal winds are ~20–30 m s^{-1} over most of the planet but reach ~130 m s^{-1} in specific latitude strips, including the equator and a narrow jet at 23°N (Simon-Miller et al. 2006). Vertical velocities are less certain but have been estimated at $\sim 10^{-5}$ m s^{-1} throughout much of the stratosphere, reaching speeds of $\sim 3 \times 10^{-4}$ m s^{-1} at high latitudes (Moreno & Sedano 1997).

To apply Equations (48), (49), and (50) to Jupiter, we adopt $f = 2.4 \times 10^{-4}$ s^{-1} (appropriate to 45° latitude), $R = 3700$ J kg^{-1} K^{-1}, $p = 0.1$ bar, and $c_p = 1.3 \times 10^4$ J kg^{-1} K^{-1}, and evaluate NH using an isothermal background temperature profile with a temperature of 165 K. Using a length scale of 10^4 km (implying $l = 6 \times 10^{-7}$ m^{-1}) and an efficiency $\eta \sim 10^{-3}$ (see footnote 13), our theory predicts $\Delta T_{\rm horiz} \sim 3$ K, $\Delta u \sim 50$ m s^{-1}, and $\overline{\varpi} \sim 1 \times 10^{-8}$ s^{-1}, which for a scale height of 20 km implies a vertical velocity of $\overline{\varpi} H \sim 2 \times 10^{-4}$ m s^{-1}. The predicted meridional temperature contrasts and horizontal wind speeds match the observations reasonably well. The predicted vertical velocity lies close to the upper end of the observationally inferred range, suggesting that our theoretical estimate may be several times larger than the actual global-mean vertical velocity (a mismatch that may result from the crudity of our parameterization of radiative heating/cooling). Over and above the specific numerical comparisons, it is worth emphasizing that observational analysis of Jupiter's stratospheric circulations supports the overall dynamical framework adopted here; the primary complication is that Jupiter (unlike brown dwarfs) exhibits a latitudinal gradient of stellar irradiation, and thus its stratosphere exhibits aspects of both thermal and mechanically driven circulations. Despite this complication, the comparison is encouraging and gives us confidence in applying the theory to brown dwarfs and directly imaged EGPs.

We next apply the theory to brown dwarfs. Figure 9 shows the solutions (48), (49), and (50) as a function of temperature and η for parameter values representative of brown dwarfs. The dominant horizontal length scale of the flow is poorly constrained, and we here adopt a wavelength of 10^4 km, similar to the jet widths on Jupiter and Saturn. For simplicity, we parameterize the mean atmospheric temperature profile in the radiative zone as vertically isothermal, which implies that $NH = R\sqrt{T/c_p}$. The magnitude of the horizontal diffusivity D is likewise poorly constrained; nevertheless, the baroclinic eddy fluxes that D parameterizes should be small if isentropes are nearly flat, which will be the case in strongly stratified regions if horizontal temperature perturbations are small compared to the mean temperature. We here set $D = 0$, yielding an upper limit on the amplitude of the horizontal temperature and winds.

Key points are as follows. First, at the ~1000 K temperatures of typical L/T dwarfs, the predicted horizontal temperature perturbations on isobars are ~5–50 K for plausible efficiencies. Notably, in the $D \to 0$ limit, the temperature perturbations at a given η are independent of length scale and rotation rate. To see why, note that the steady state results from a balance between forcing (energy input) and damping (energy removal). Energy input is represented by η; in the model assumed here, energy damping results solely from loss of potential energy by radiative relaxation, and for a given value of $\tau_{\rm rad}$, this energy damping depends on $\Delta T_{\rm horiz}$ but is independent of the rotation rate and flow length scales. The temperature perturbations in Figure 9 are much less than the mean temperature, which, given plausible stratifications, suggests that isentropes are relatively flat. This provides tentative a posteriori justification for neglecting D, as horizontal energy fluxes due to baroclinic eddies—which is what D represents—tend to be modest under such conditions.

Second, Figure 9 suggests that large-scale, organized horizontal wind speeds of tens to hundreds of m s^{-1} are plausible for L/T dwarfs. The speeds predicted here are similar to those suggested from analysis of brown-dwarf variability (Artigau et al. 2009; Radigan et al. 2012), which range from tens to hundreds of m s^{-1}. Unlike temperature differences, the predicted wind speeds depend on length scale and rotation rate. This is most clearly seen from the thermal-wind relationship (42): for a given $\Delta T_{\rm horiz}$, shorter length scales imply larger horizontal pressure-gradient forces, requiring larger wind speed to maintain geostrophy. Likewise, a slower rotation rate implies weaker Coriolis forces for a given wind speed; to balance a given pressure-gradient force, faster winds would be needed at slower rotation rates. At large scales, these winds will comprise stratified, geostrophically balanced turbulence, possibly organized into coherent structures such as vortices or zonal jets.

Third, for plausible efficiencies, our theory predicts large-scale vertical velocities of $\sim 10^{-6}$ to 10^{-5} scale heights per second (Figure 9). Typical times for air parcels to ascend or descend over a scale height are therefore $\sim 10^5$–10^6 s. For a typical brown-dwarf scale height of 7 km, this implies vertical velocities of ~0.01–0.1 m s^{-1}. Importantly, this motion is not diffusive but is coherent vertically, comprising the ascending/descending branches of a large-scale overturning circulation. We emphasize that these vertical motions occur within the *stratified* regions above the radiative–convective boundary and are distinct from the convection below the radiative–convective boundary.

Such a wave-driven overturning circulation differs fundamentally from a thermally driven circulation such as a Hadley cell. Because the horizontal temperature differences result primarily from vertical advection of the background vertical entropy gradient, the model implies that on isobars, the ascending regions are *cold* and descending regions are *hot*. This thermally indirect configuration results from the fact that the circulation is mechanically rather than thermally driven. Such thermally indirect, wave-driven circulations are generic features of planetary upper tropospheres and stratospheres. On Earth, the main overturning circulation in the stratosphere, the Brewer–Dobson circulation, is just such a phenomenon (for reviews, see Haynes 2005; Vallis 2006, Chapter 13). Likewise, in Jupiter's upper troposphere, observations indicate the existence of ascending motion in the cold, cloudy "zones" and descending motion in the warmer, less cloudy "belts" (Gierasch et al. 1986; West et al. 1992). Of course, in the brown-dwarf context, we have neglected the potentially important roles of latent heating and radiative feedbacks involving clouds, which may complicate the picture.

In summary, our theory predicts that the stratified atmospheres of brown dwarfs and giant planets will generically

contain geostrophic flows accompanied by a large-scale overturning circulation, both driven by the absorption of waves propagating from near the radiative–convective boundary. This overturning circulation comprises coherent, large-scale horizontal *and vertical* motions despite the stratified thermal structure. The vertical entropy advection caused by this overturning motion generates large-scale horizontal temperature differences.

5. OBSERVATIONAL IMPLICATIONS

5.1. Clouds and Light-curve Variability

Our results suggest horizontal temperature variations (on isobars) in the stratified atmosphere up to ∼50 K, and even in the absence of clouds, these variations could cause light curve variability. The blackbody flux from a region with a photospheric temperature $T + \Delta T_{\rm horiz}$ differs from that in a region of photospheric temperature T by $\Delta F \sim 4\sigma T^3 \Delta T_{\rm horiz}$, implying that the fractional broadband flux variations emitted by different regions of the brown dwarf, due to thermal variations alone, are $\Delta F/F \sim 4\Delta T_{\rm horiz}/T$. For a mean temperature $T \sim 1000$ K, the fractional temperature variations are ∼0.005–0.05, and $\Delta F/F \sim 0.02$–0.2. Of course, if the atmospheric features are much smaller than the radius of the brown dwarf, these variations will largely cancel and produce minimal variation in the disk-integrated flux on rotational timescales. However, if the dominant length scales approach a brown-dwarf radius, these results suggest that thermal variations alone could produce variations in the flux of up to a few percent on rotation timescales. This might be relevant to brown dwarfs where cloud condensation is not expected to occur at and above the photosphere (e.g., on Y and late T dwarfs).

Our models suggest that when cloud condensation levels lie in the atmosphere, patchy clouds will form that could lead to significant variability. Freytag et al. (2010) predicted cloud patchiness at very small scales due to fluctuating gravity waves, but such small-scale fluctuations will cancel out in a disk average and thus will not produce light curve variations. In contrast, our models predict *large-scale*, vertically coherent regions of ascent and descent associated with geostrophically balanced, turbulent structures such as large vortices, with time-mean vertical velocities up to ∼0.1 m s^{-1}. Importantly, these vertical motions occur despite the fact that the atmosphere is stably stratified. Regions of ascent promote cloud formation, whereas regions of descent transport dry air from above and inhibit cloud formation—just as occurs with the cloudy zones and less cloudy belts on Jupiter. Near typical photospheric pressures of ∼1 bar, the continuum particle-settling regime is approximately valid; if particles settle following Stokes flow, then the timescale to settle vertically by a scale height exceeds ∼10^5–10^6 s for particle sizes less than about 1 μm.[14] Thus, given our predicted vertical velocities, particles with radii less than ∼1 μm can remain suspended in regions of large-scale ascent, with regions of large-scale descent exhibiting lower cloud abundances. Such large-scale cloud patchiness can lead to significant light curve variability as cloudy and relatively cloud-free regions rotate into and out of view.

How does the vertical scale of any cloud layers relate to that of the circulation itself? As mentioned previously, the atmospheric circulation is likely to extend coherently over vertical distances of a scale height or more. To understand the vertical scale of the cloud layer, consider a single condensable species that is saturated. From the Clausius–Clapeyron equation, it can be shown that the ratio of the scale height of the condensable vapor, H_v, to the atmospheric pressure scale height, H, is

$$\frac{H_v}{H} \approx \frac{R_v T}{L\,\Delta \ln T_{\rm sh}}, \tag{52}$$

where R_v and L are the specific gas constant and latent heat of the condensable species, T is temperature, and $\Delta \ln T_{\rm sh}$ is the temperature change of the background temperature profile over a scale height. For a dry adiabat, $\Delta \ln T_{\rm sh} = R/c_p$, where R and c_p are the specific gas constant and specific heat of the background air. Adopting parameters for iron condensation ($R_v = 149$ J kg^{-1} K^{-1} and $L \approx 6 \times 10^6$ J kg^{-1}), $T \approx 1000$ K, along with $\Delta \ln T_{\rm sh} = R/c_p \approx 2/7$ for a diatomic, H_2 atmosphere, we obtain $H_v/H \approx 0.09$. Therefore, if the temperature profile is close to an adiabat, the condensation layer is extremely thin compared to a scale height. Particles that condense in this layer will gravitationally settle; particles that settle faster than the upward vertical transport rate will be confined to a vertically thin layer, but particles that settle more slowly than the upward vertical transport rate may be advected into a vertically extended haze layer. Nevertheless, if the background temperature profile is closer to an isotherm, Equation (52) indicates that even the condensation layer itself could become vertically extended.

These arguments suggest the following picture for the dust cycle in the presence of a large-scale atmospheric circulation. In regions of ascent, coherent upward motions will bring fresh material upward to the condensation level, leading to condensation and dust formation. Extremely small particles could be advected upward with the flow, but large particles will gravitationally settle, leading to a vertically thin cloud deck in the ascending regions. The gas in the ascending regions will therefore become depleted in condensate as it rises beyond the condensation level. In the upper part of the circulation, this ascending air will presumably move horizontally and begin to descend (Figure 8). Assuming that the circulation extends sufficiently far above the condensation level, the regions of descending air will therefore be depleted in condensate, leading to large-scale "holes" in the cloud deck—at least in the horizontal distribution of large particles. In contrast, small particles that have settling times longer than the circulation times may form a quasi-ubiquitous, unbroken haze layer. As a result, the particle size distribution may vary significantly not only vertically but horizontally as well. Particles advected downward with the flow in the descending regions—or that are sufficiently large to settle in the ascending regions, despite the upward airflow there—will sublimate, leading to an overall mass balance between condensation and sublimation. Even though we are emphasizing here the large-scale organization, the dust layer could also exhibit patchiness at small scales, particularly

[14] For temperatures and molecular viscosities appropriate to L/T dwarfs, gas kinetic effects cause a significant deviation from Stokes fall speeds only at pressures less than ∼0.1 bar, indicating that Stokes settling represents a reasonable approximation near the IR photosphere. The Stokes settling velocity is $w_{\rm settle} = 2\Delta\rho g a^2/9\mu$, where $\Delta\rho$ is the density difference between the particles and air, g is gravity, a is particle radius, and μ is the dynamic viscosity of H_2 air. Equating this fall speed to the mean vertical wind speed $H\overline{\varpi}$ leads to the condition that particles can remain suspended if the particle size

$$a \lesssim \left(\frac{9\mu H\overline{\varpi}}{2\Delta\rho g}\right)^{1/2}. \tag{51}$$

Adopting a viscosity of 2×10^{-5} Pa s appropriate to H_2 at 1000 K (Ackerman & Marley 2001), $\Delta\rho = 3000$ kg m^{-3}, $g = 500$ m s^{-1}, $H = 5$ km, and $\overline{\varpi} = 10^{-6}$–$10^{-5}$ s^{-1} yields the condition $a \lesssim 0.5$–2 μm for particles to remain suspended.

if latent heating is dynamically important (as occurs in cumulus clouds on Earth).

Jupiter and Saturn represent prime examples of exactly this type of cycle, with ammonia serving as the condensate. Jupiter's bright cloud bands, called "zones," are regions of large-scale ascent at and above the ammonia cloud deck and exhibit large mean cloud opacity. Jupiter's darker cloud bands, called "belts," are regions of large-scale descent at and above the clouds (e.g., Gierasch et al. 1986; Carlson et al. 1994) and exhibit smaller mean cloud opacity. Anticyclonic vortices like the Great Red Spot also appear to be regions of mean large-scale ascent and exhibit a cloud deck with greater optical depth, and extending to greater altitude, than the cloud deck in surrounding regions. At horizontal scales of 10^3–10^4 km, Jupiter's and Saturn's cloud decks are quite patchy in particles several microns or larger—as evident in 5 μm images of either planet—but relatively more uniform in particles smaller than a micron (e.g., West et al. 1986). Both belts and zones exhibit significant small-scale patchiness superposed on top of this large-scale structure (Banfield et al. 1998).

The large-amplitude light-curve variations observed by Artigau et al. (2009) and Radigan et al. (2012) exhibit not only variation on rotational timescales but also qualitative changes to the *shape* of the rotational modulation over many rotation periods. This motivates a consideration of the range of dynamical timescales operating in the atmosphere of brown dwarfs. Given our predicted vertical velocities and typical horizontal scales of $L \sim 10^4$ km, the horizontal advection time $\tau_{\rm adv} \sim L/U \sim 10^5$–$10^6$ s. For a typical brown-dwarf rotation period of $\sim 10^4$ s, this suggests that qualitative, order-unity changes to the circulation (e.g., in the locations or shapes of vortices and detailed structure of the turbulence) occur on timescales of typically ~10–100 rotation periods. This is qualitatively consistent with the timescales over which major changes to the light-curves are seen in observations (e.g., Artigau et al. 2009).

5.2. Vertical Mixing

A variety of brown dwarfs, including Gl 229B, Gl 570D, HD 3561B, and 2MASS J0415−0935, as well as directly imaged planets such as those orbiting HR 8799 and 2M1207, show evidence for disequilibrium abundances of CO, CH_4, and/or NH_3 (e.g., Noll et al. 1997; Saumon et al. 2000, 2006, 2007; Stephens et al. 2009; Leggett et al. 2007a, 2007b, 2008; Hinz et al. 2010; Barman et al. 2011a, 2011b; Marley et al. 2012). Interestingly, in some of these cases, models suggest that the quenching of CO occurs in the radiative zone rather than the convection zone, implying that vertical mixing in the stratified atmosphere is necessary to explain the observations. Generally, these 1D models parameterize the mixing as an eddy diffusion and tune the diffusion coefficient to provide a match between synthetic and observational IR spectra. Recently, Visscher & Moses (2011) showed, using updated reaction kinetics and estimates of quench timescales, that several of these studies underestimated the eddy diffusivities necessary to explain the inferred CO abundances; as a case study, they showed that an eddy diffusivity exceeding $\sim 10^2$ m^2 s^{-1} is necessary to explain the CO abundance on Gl 229B.

Freytag et al. (2010) demonstrate one mechanism for mixing in the stratified atmosphere, which is the vertical mixing induced by breaking gravity waves. Our models in Section 4 suggest an alternate mechanism: that the mixing results from the large-scale, wave-driven circulation. Our models predict transport times over a scale height of $\tau_{\rm vert} \sim 10^5$–$10^6$ s for a typical L/T dwarf (see Figure 9). As described in Section 4, these motions are not diffusive but comprise vertically coherent advection extending potentially across several scale heights. At the temperatures appropriate for typical L/T-dwarf atmospheres, CO⇌CH_4 chemical interconversion timescales at low pressure exceed these transport timescales (Cooper & Showman 2006; Visscher & Moses 2011), indicating that the wave-driven circulation can induce chemical quenching of CO and CH_4.

The key point is that waves can cause two distinct mechanisms of vertical transport: direct vertical mixing associated with the wave breaking, and vertical transport by a large-scale circulation driven by wave interactions with the mean flow. Which is larger depends on the wave spectrum, the detailed structure of the horizontal wind, the atmospheric stratification, and other properties. In Earth's stratosphere and lower mesosphere, vertical mixing by the large-scale (meridional) overturning circulation dominates over that caused by wave breaking (Holton 1983; Holton & Schoeberl 1988), but the reverse may be true at even higher altitudes, in the upper mesosphere. Detailed calculations will be necessary to evaluate the relative transport efficiency of the two mechanisms in the context of brown dwarfs.

6. CONCLUSIONS

We have demonstrated that brown dwarfs should exhibit vigorous atmospheric circulations at regional to global scales, and that this circulation will shape the cloudiness, light-curve variability, and vertical mixing inferred in their atmospheres. Our main findings are as follows.

1. Given inferred rotation rates and plausible wind speeds, the circulation on cool brown dwarfs at scales larger than thousands of kilometers will be rotationally dominated, exhibiting a horizontal force balance between pressure-gradient and Coriolis forces (geostrophic balance). The rapid rotation will control many aspects of the dynamical behavior at large scales.
2. Using standard vorticity and angular-momentum arguments, we showed that in the convective interior, the rapid rotation and nearly isentropic conditions will lead to velocities and convective structure aligned—at large scales—along columns parallel to the rotation axis. We presented global, 3D, anelastic numerical simulations of convection in brown-dwarf interiors that confirm this prediction. At large scales, convective velocities in the deep interior are affected significantly by the rotation, leading to a different prediction for the scaling of convective velocities with heat flux than predicted by standard (non-rotating) mixing length theory.
3. Our 3D convection models show that convection occurs more efficiently at high latitudes than at low latitudes, and this can lead to a systematic equator-to-pole temperature difference in the upper convective zone that may reach ~1 K. The convection develops significant regional-scale structure likely to affect the overlying atmosphere in an observable manner. Scaling arguments suggest that due to Lorentz-force braking in the deep, electrically conducting regions, and due to modest thermal-wind shear in the outermost (molecular) part of the convection zone, the horizontal winds in the convection zone at large scales will be modest (probably less than $\sim 10^2$ m s^{-1}).
4. The interaction of convection with the overlying, stably stratified atmosphere will generate a wealth of atmospheric

waves, and we argue that, just as in the stratospheres of planets in the solar system, the interaction of these waves with the mean flow will lead to a significant atmospheric circulation at regional to global scales. At horizontal scales exceeding thousands of kilometers, such a wave-driven circulation will, to good approximation, be geostrophically balanced and may consist of large-scale stratified turbulence, vortices, and/or jets. The geostrophic flow will be accompanied by a large-scale overturning ("meridional") circulation that acts to maintain geostrophy.

5. We presented a simple analytic theory of this wave-driven atmospheric circulation which illuminates the dynamical mechanisms and enables order-of-magnitude estimates for the characteristic horizontal temperature differences, wind speeds, and vertical mixing rates as a function of the amplitude of the wave driving, the mean stratification of the atmosphere, and other properties. For plausible wave-driving efficiencies, this theory predicts that at photospheric pressures, the circulation will comprise horizontal temperature variations of several to $\sim$50 K, horizontal wind speeds of $\sim$10–300 m s^{-1}, and vertical velocities that advect air over a scale height in timescales of $\sim 10^5$–10^6 s.
6. These models help to explain recent evidence for atmospheric circulation on cool brown dwarfs. Our predicted large-scale vertical motion in the stratified atmosphere would lead to cloud formation and mix chemical constituents vertically, helping to explain the quenching of CO, CH_4, and NH_3 inferred on many brown dwarfs. This overturning circulation is *spatially organized,* consisting of coherent, large-scale regions of ascent and descent, indicating the likelihood of cloud patchiness that could explain light-curve variability (Artigau et al. 2009; Radigan et al. 2012; Buenzli et al. 2012). Wind speeds of plausibly tens to hundreds of m s^{-1} would advect cloudy and cloud-free regions horizontally, leading to significant changes in the *shape* of light curves over typically tens of rotation periods or more.

Our models are of course highly idealized, and there remains a pressing need for detailed, 3D simulations of the atmospheric circulation and its interaction with the convective interior. Coupling of such models to prescriptions of radiative transfer and cloud formation will be necessary not only to explain the particular shapes and amplitudes of brown-dwarf light curves as a function of wavelength but also to understand the role of the atmospheric circulation in influencing the L/T transition. Future observations and models are likely to lead to major new insights over the next few years.

This research was supported by Planetary Atmospheres grant NNX10AB91G, Origins grant NNX12AI79G, and NSF grant AST1313444 to A.P.S. and by a Marie Curie Career Integration grant (CIG-304202) to Y.K. A.P.S. thanks the Helen Kimel Center for Planetary Science at the Weizmann Institute of Science for financial support and a stimulating environment in which to initiate this project.

REFERENCES

Ackerman, A. S., & Marley, M. S. 2001, ApJ, 556, 872
Adcroft, A., Campin, J.-M., Hill, C., & Marshall, J. 2004, MWRv, 132, 2845
Allard, F., Hauschildt, P. H., Alexander, D. R., Tamanai, A., & Schweitzer, A. 2001, ApJ, 556, 357
Andrews, D. G., Holton, J. R., & Leovy, C. B. 1987, Middle Atmosphere Dynamics (New York: Academic)
Arakawa, A., & Lamb, V. 1977, MComP, 17, 173
Artigau, É., Bouchard, S., Doyon, R., & Lafrenière, D. 2009, ApJ, 701, 1534
Aurnou, J. M., & Olson, P. L. 2001, GeoRL, 28, 2557
Baldwin, M. P., Gray, L. J., Dunkerton, T. J., et al. 2001, RvGeo, 39, 179
Banfield, D., Gierasch, P. J., Bell, M., et al. 1998, Icar, 135, 230
Barman, T. S., Macintosh, B., Konopacky, Q. M., & Marois, C. 2011a, ApJ, 733, 65
Barman, T. S., Macintosh, B., Konopacky, Q. M., & Marois, C. 2011b, ApJL, 735, L39
Bézard, B., Lellouch, E., Strobel, D., Maillard, J.-P., & Drossart, P. 2002, Icar, 159, 95
Boubnov, B. M., & Golitsyn, G. S. 1990, JFM, 219, 215
Bowler, B. P., Liu, M. C., Dupuy, T. J., & Cushing, M. C. 2010, ApJ, 723, 850
Buenzli, E., Apai, D., Morley, C. V., et al. 2012, ApJL, 760, L31
Burgasser, A. J., Marley, M. S., Ackerman, A. S., et al. 2002, ApJL, 571, L151
Burrows, A., Hubbard, W. B., Lunine, J. I., & Liebert, J. 2001, RvMP, 73, 719
Burrows, A., Marley, M., Hubbard, W. B., et al. 1997, ApJ, 491, 856
Burrows, A., Sudarsky, D., & Hubeny, I. 2006a, ApJ, 640, 1063
Burrows, A., Sudarsky, D., & Hubeny, I. 2006b, ApJ, 650, 1140
Busse, F. H. 1976, Icar, 29, 255
Busse, F. H. 2002, PhFl, 14, 1301
Carlson, B. E., Lacis, A. A., & Rossow, W. B. 1994, JGR, 99, 14623
Chabrier, G., Baraffe, I., Allard, F., & Hauschildt, P. 2000, ApJ, 542, 464
Cho, J. Y.-K., & Polvani, L. M. 1996, Sci, 8, 1
Christensen, U. R. 2001, GeoRL, 28, 2553
Christensen, U. R. 2002, JFM, 470, 115
Christensen, U. R. 2010, SSRv, 152, 565
Christensen, U. R., & Aubert, J. 2006, GeoJI, 166, 97
Christensen, U. R., Holzwarth, V., & Reiners, A. 2009, Natur, 457, 167
Clayton, D. D. 1968, Principles of Stellar Evolution and Nucleosynthesis (New York: McGraw-Hill)
Cooper, C. S., & Showman, A. P. 2006, ApJ, 649, 1048
Currie, T., Burrows, A., Itoh, Y., et al. 2011, ApJ, 729, 128
Cushing, M. C., Kirkpatrick, J. D., Gelino, C. R., et al. 2011, ApJ, 743, 50
Cushing, M. C., Roellig, T. L., Marley, M. S., et al. 2006, ApJ, 648, 614
Dritschel, D. G., & McIntyre, M. E. 2008, JAtS, 65, 855
Dritschel, D. G., & Scott, R. K. 2011, RSPTA, 369, 754
Fegley, B., Jr., & Lodders, K. 1996, ApJL, 472, L37
Fernando, H. J. S., Chen, R.-R., & Boyer, D. L. 1991, JFM, 228, 513
Freytag, B., Allard, F., Ludwig, H.-G., Homeier, D., & Steffen, M. 2010, A&A, 513, A19
Friedson, A. J. 1999, Icar, 137, 34
Galicher, R., Marois, C., Macintosh, B., Barman, T., & Konopacky, Q. 2011, ApJL, 739, L41
Gierasch, P. J., Magalhaes, J. A., & Conrath, B. J. 1986, Icar, 67, 456
Gilman, P. A., & Glatzmaier, G. A. 1981, ApJS, 45, 335
Glatzmaier, G. A., Evonuk, M., & Rogers, T. M. 2009, GApFD, 103, 31
Goldreich, P., & Kumar, P. 1990, ApJ, 363, 694
Golitsyn, G. S. 1980, DoSSR, 251, 1356
Golitsyn, G. S. 1981, DoSSR, 261, 317
Griffith, C. A., & Yelle, R. V. 1999, ApJL, 519, L85
Grote, E., Busse, F. H., & Tilgner, A. 2000, PEPI, 117, 259
Guillot, T., & Morel, P. 1995, A&AS, 109, 109
Guillot, T., Stevenson, D. J., Hubbard, W. B., & Saumon, D. 2004, in Jupiter: The Planet, Satellites and Magnetosphere, ed. F. Bagenal, T. E. Dowling, & W. B. McKinnon (Cambridge: Cambridge Univ. Press), 35
Haynes, P. 2005, AnRFM, 37, 263
Haynes, P. H., McIntyre, M. E., Shepherd, T. G., Marks, C. J., & Shine, K. P. 1991, JAtS, 48, 651
Heimpel, M., Aurnou, J., & Wicht, J. 2005, Natur, 438, 193
Hinz, P. M., Rodigas, T. J., Kenworthy, M. A., et al. 2010, ApJ, 716, 417
Holton, J. R. 1983, JAtS, 40, 2497
Holton, J. R. 2004, An Introduction to Dynamic Meteorology (4th ed.; San Diego, CA: Academic)
Holton, J. R., & Schoeberl, M. R. 1988, JGR, 93, 11075
Huang, H.-P., & Robinson, W. A. 1998, JAtS, 55, 611
Hubeny, I., & Burrows, A. 2007, ApJ, 669, 1248
Ingersoll, A. P. 1990, Sci, 248, 308
Ingersoll, A. P., & Pollard, D. 1982, Icar, 52, 62
James, I. N. 1994, Introduction to Circulating Atmospheres (Cambridge Atmospheric and Space Science Series; Cambridge: Cambridge Univ. Press)
Jones, C. A., & Kuzanyan, K. M. 2009, Icar, 204, 227
Kaspi, Y. 2008, PhD thesis, Massachusetts Institute of Technology
Kaspi, Y., Flierl, G. R., & Showman, A. P. 2009, Icar, 202, 525
Kirk, R. L., & Stevenson, D. J. 1987, ApJ, 316, 836
Kirkpatrick, J. D. 2005, ARA&A, 43, 195
Kirkpatrick, J. D., Reid, I. N., Liebert, J., et al. 1999, ApJ, 519, 802

Knapp, G. R., Leggett, S. K., Fan, X., et al. 2004, AJ, 127, 3553
Leggett, S. K., Burningham, B., Saumon, D., et al. 2010, ApJ, 710, 1627
Leggett, S. K., Marley, M. S., Freedman, R., et al. 2007a, ApJ, 667, 537
Leggett, S. K., Saumon, D., Albert, L., et al. 2008, ApJ, 682, 1256
Leggett, S. K., Saumon, D., Marley, M. S., et al. 2007b, ApJ, 655, 1079
Liu, J., Goldreich, P. M., & Stevenson, D. J. 2008, Icar, 196, 653
Liu, J., & Schneider, T. 2010, JAtS, 67, 3652
Madhusudhan, N., Burrows, A., & Currie, T. 2011, ApJ, 737, 34
Marcus, P. S., Kundu, T., & Lee, C. 2000, PhPl, 7, 1630
Marley, M. S., Saumon, D., Cushing, M., et al. 2012, ApJ, 754, 135
Marley, M. S., Saumon, D., & Goldblatt, C. 2010, ApJL, 723, L117
Marley, M. S., Saumon, D., Guillot, T., et al. 1996, Sci, 272, 1919
Marley, M. S., Seager, S., Saumon, D., et al. 2002, ApJ, 568, 335
Miesch, M. S., & Toomre, J. 2009, AnRFM, 41, 317
Moreno, F., & Sedano, J. 1997, Icar, 130, 36
Nellis, W. J. 2000, P&SS, 48, 671
Nellis, W. J. 2006, RPPh, 69, 1479
Nellis, W. J., Ross, M., & Holmes, N. C. 1995, Sci, 269, 1249
Nellis, W. J., Weir, S. T., & Mitchell, A. C. 1996, Sci, 273, 936
Noll, K. S., Geballe, T. R., & Marley, M. S. 1997, ApJL, 489, L87
Nozawa, T., & Yoden, S. 1997, PhFl, 9, 2081
Ogura, Y., & Phillips, N. A. 1962, JAtS, 19, 173
Pedlosky, J. 1987, Geophysical Fluid Dynamics (2nd ed.; New York: Springer)
Peixoto, J. P., & Oort, A. H. 1992, Physics of Climate (New York: American Institute of Physics)
Prinn, R. G., & Barshay, S. S. 1977, Sci, 198, 1031
Radigan, J., Jayawardhana, R., Lafrenière, D., et al. 2012, ApJ, 750, 105
Reiners, A., & Basri, G. 2008, ApJ, 684, 1390
Reiners, A., & Christensen, U. R. 2010, A&A, 522, A13
Rogers, T. M., Lin, D. N. C., & Lau, H. H. B. 2012, ApJL, 758, L6
Saumon, D., Chabrier, G., & van Horn, H. M. 1995, ApJS, 99, 713
Saumon, D., Geballe, T. R., Leggett, S. K., et al. 2000, ApJ, 541, 374
Saumon, D., & Marley, M. S. 2008, ApJ, 689, 1327
Saumon, D., Marley, M. S., Cushing, M. C., et al. 2006, ApJ, 647, 552
Saumon, D., Marley, M. S., Leggett, S. K., et al. 2007, ApJ, 656, 1136
Scott, R. K., & Polvani, L. 2007, JAtS, 64, 3158
Shepherd, T. G. 2000, JASTP, 62, 1587
Shepherd, T. G. 2003, Chem. Rev., 103, 4509
Showman, A. P. 2007, JAtS, 64, 3132
Showman, A. P., Cho, J. Y.-K., & Menou, K. 2010, in Exoplanets, ed. S. Seager (Tucson, AZ: Univ. Arizona Press), 471
Showman, A. P., & Guillot, T. 2002, A&A, 385, 166
Showman, A. P., Kaspi, Y., & Flierl, G. R. 2011, Icar, 211, 1258
Simon-Miller, A. A., Conrath, B. J., Gierasch, P. J., et al. 2006, Icar, 180, 98
Skemer, A. J., Close, L. M., Szűcs, L., et al. 2011, ApJ, 732, 107
Smith, K. S. 2004, JAtS, 61, 1420
Smith, K. S., & Vallis, G. K. 2001, JPO, 31, 554
Starchenko, S. V., & Jones, C. A. 2002, Icar, 157, 426
Stephens, D. C., Leggett, S. K., Cushing, M. C., et al. 2009, ApJ, 702, 154
Stevenson, D. J. 1979, GApFD, 12, 139
Stevenson, D. J. 2003, E&PSL, 208, 1
Stevenson, D. J. 2010, SSRv, 152, 651
Tsuji, T. 2002, ApJ, 575, 264
Vallis, G. K. 2006, Atmospheric and Oceanic Fluid Dynamics: Fundamentals and Large-Scale Circulation (Cambridge: Cambridge Univ. Press)
Vasavada, A. R., & Showman, A. P. 2005, RPPh, 68, 1935
Visscher, C., & Moses, J. I. 2011, ApJ, 738, 72
Weir, S. T., Mitchell, A. C., & Nellis, W. J. 1996, PhRvL, 76, 1860
West, R. A., Friedson, A. J., & Appleby, J. F. 1992, Icar, 100, 245
West, R. A., Strobel, D. F., & Tomasko, M. G. 1986, Icar, 65, 161
Zapatero Osorio, M. R., Martín, E. L., Bouy, H., et al. 2006, ApJ, 647, 1405